

Multi-phase Thermal-hydrological Processes in the Single Heater Test at Yucca Mountain

Y.W. Tsang and J.T. Birkholzer
Earth Sciences Division
E. O. Lawrence Berkeley National Laboratory
Berkeley, CA, 94720

Abstract

The Single Heater Test (SHT) is one of two *in-situ* thermal tests included in the site characterization program for the potential underground nuclear waste repository at Yucca Mountain. Coupled thermal-hydrological-mechanical-chemical processes in the fractured rock mass around the heater were monitored by numerous sensors emplaced among 30 boreholes. The change of moisture content in the rock mass was probed by periodic active testing of cross-hole radar tomography, neutron logging, electrical resistivity tomography, and interference air permeability tests. Thermal-hydrological processes in the SHT have been simulated using a 3-D numerical model and compared to the monitored data. The good agreement between the temperature data and simulated results indicates that the thermal-hydrological responses of the SHT in the 9 months of heating are well represented by the coupled thermal-hydrological numerical model. The dominant heat transfer process is by conduction, and the signature of vapor and liquid counter flow is subtle in the temperature data. The simulated result for a dry-out zone of about 1 m around the heater hole, and a condensation zone of increased liquid saturation outside of the dry-out zone, is consistent with the radar tomography and air permeability data. Active testing data also indicate that the moisture content is larger below than above the heater horizon, suggesting gravity drainage. Model studies show that gravity drainage occurs in simulations using the dual permeability conceptual model; but is absent in the effective continuum model, where matrix and fractures are required to be in thermodynamic equilibrium at all times.

1. Introduction

As part of the Yucca Mountain Site characterization program, thermal tests are being carried out in the potential repository formation of Topopah Spring welded tuff in the Exploratory Studies Facility (ESF). The primary objective of the ESF Thermal Tests is to develop a better understanding of the coupled thermal, mechanical, hydrological, and chemical processes likely to exist in the rock mass surrounding the potential geological repository at Yucca Mountain. These coupled processes determine the waste package environment whose characteristics control the

corrosion of waste canisters and the mobilization rate of radionuclides. The coupled processes also play an important role in the possible migration of radionuclides away from the potential repository into the environment.

The *in situ* thermal test program includes the Single Heater Test (SHT), and the Drift Scale Test. The SHT consists of a 5-m-long heating element, at a nominal 4 kW, emplaced horizontally among 30 instrumental boreholes spanning a rock block of approximately 13 m x 10 m x 13 m. The heating of the SHT was initiated in August 1996, and ended after 9 months. Currently, the cooling phase is being monitored. The SHT is intended to serve as a shakedown test for the DST with a much larger scale and longer duration. The start date for DST was December 1997, for a heating period of 4 years. The scope of the shakedown includes practicing testing methods, perfecting data acquisition logistics, and applying modeling and data interpretation methods.

The scientific responsibility of fielding and interpreting the thermal tests is shared among several organizations, including the Sandia National Laboratories (SNL), the Lawrence Livermore National Laboratory (LLNL), and Ernest Orlando Lawrence Berkeley National Laboratory (LBNL), under the coordination of the Civilian Radioactive Waste Management System Management and Operating Contractor (CRWMS M&O). At the time of writing, the heating phase data of the SHT have been evaluated and analyzed by the thermal testing teams of the three national laboratories (CRWMS M&O, 1997). In this paper, the focus is on the contribution from LBNL toward understanding the multi-phase thermal-hydrological response of the heating phase of the SHT. A 3-D numerical model of the SHT was developed to simulate the coupled transport of water, vapor, air, and heat in the rock mass surrounding the heater. The simulated results for different conceptual models of the SHT are compared to measured data. Sensitivity of the thermohydrological behavior of the SHT to certain key hydrological parameters of the unsaturated flow regime is studied.

While modeling studies of the thermal-hydrological conditions of a high-level nuclear waste repository at Yucca Mountain exist in the literature (e.g., Tsang and Pruess, 1987; Pruess et al., 1990; Buscheck and Nitao, 1992; Buscheck and Nitao, 1993; Buscheck et al., 1993; Pruess and Tsang, 1994), the *in situ* thermal tests present a unique opportunity to evaluate our understanding to date of the coupled processes against measurements in the natural setting of the repository

rocks. Predictive modeling of the thermal test was performed and documented prior to the start of the SHT heating (Birkholzer and Tsang, 1996), and as measured data became available, the pre-test models were refined and calibrated. It is by the iterative process of interpretative modeling against data that we build confidence in our understanding of the complex coupled processes involved, and thus in our ability to predict the performance of the waste repository.

2. Test Configuration and Thermal-Hydrological Processes

The SHT block resides in the middle non-lithophysal unit of the Topopah Spring welded tuff approximately 200 m above the groundwater table. Though the welded tuff has very low matrix permeability, it is intensely fractured, with the fracture permeability several orders of magnitude higher than the matrix permeability. At ambient state, with the current estimates of the average percolation flux of up to tens of millimeters per year (Flint et al., 1997) at the repository horizon, the fractures are essentially drained and not very conductive for water. However, strong capillary forces hold a significant amount of water in the matrix pores, which have a liquid saturation of about 92 % at the SHT location (Tsang et al., 1996; Wang and Suárez-Rivera, 1997). This water can be mobilized from heating of the rock mass, raising the liquid saturation in the fractures. Then the water flux in the fractures can be enhanced by several orders of magnitude from its ambient values.

Figure 1 shows the layout and borehole arrangement for the SHT. Figure 1a presents a schematic 3-D view of the boreholes, color coded according to their different functions, and Figure 1b shows both the plan view and a cross-section. The SHT block is surrounded by the Observation Drift to the north, the Thermomechanical Alcove to the west, and the Thermomechanical Alcove Extension to the south. A 4-kW heater of 5 m length has been placed in the horizontal borehole collared on the west wall, at 2 m above the drift floor. The near end of the heater is located approximately 2 m into the rock from the wall. All coordinates are given relative to the location of the heater hole, where the origin of the coordinate system is chosen to coincide with the center of the Borehole 1 collar.

The coupled thermal-hydrological processes are monitored by a multitude of sensors installed in the numerous instrumented boreholes to measure the temperature, humidity, gas pressure, mechanical displacement, and stresses of the rock mass in response to the generated heat. There are 530 sensors in the SHT that measure the thermal (333), mechanical (45), hydrological (52), and/or chemical (100) data. These passive monitoring data are recorded by a data collection system on at least an hourly basis.

The expected rock mass' thermal-hydrological response to the heater power output is the drying of the rock immediately surrounding the heater, the carrying away of moisture vapor from the heated area, the condensation of the vapor in the cooler regions of the rock mass farther away from the single heater, the possible return of water to the vicinity of the heating due to capillary suction, and the possible drainage of water away from the heated area due to gravity. The results of vaporization, drying, condensation and rewetting processes are reflected in the spatial variation and temporal evolution of the liquid saturation in the rock mass. To probe the changes in the rock mass moisture content, active testing by neutron logging, electrical resistivity tomography, cross-hole radar tomography, and interference air permeability measurements are carried out in selected boreholes (labeled as hydrological in Figure 1a) at appropriate intervals throughout the heater test (CRWMS M&O, 1997). Both the passive monitoring and active testing data will be considered in the analysis and interpretation of SHT.

Most of the key processes potentially involved in the thermal-hydrological response of the unsaturated fractured tuff to heat are reviewed here with the help of a schematic diagram (Figure 2). As the formation temperatures approach 100 °C around the heater, matrix pore water boils and vaporizes. Most of the vapor generated moves into the fractures, where it becomes highly mobile and is driven with the gas pressure gradient away from the heat source. When the vapor encounters cooler rock, it condenses, and the local fracture saturation builds up. Part of the condensate may then imbibe into the matrix, where it is subject to a very strong capillary gradient towards the heat source, giving rise to a reflux of liquid to the dry-out areas. If matrix imbibition is relatively slow, the condensate may also remain in the fractures and eventually become mobile. Some fraction of the condensate in the fractures may flow back towards the boiling zone; however, as capillary forces are relatively weak in the fractures, a substantial amount of liquid may drain from the heater by gravity. Occurrence of gravity drainage depends on the strength of

evaporation-condensation and fracture-matrix interflow behavior. The stronger the vapor flux away from the heater and the condensate reflux towards the heater, the more obvious will be the “heat pipe” signature in the temperature data (namely, a small temperature gradient), and with time, the temperature remains at the nominal boiling point. It is possible that particular matrix and fracture hydrological properties can give rise to such strong condensate reflux that a stable heat-pipe extends all the way to the heater, preventing the drying of rock and keeping the temperatures near or below 100 °C.

3. Pre-Heating Characterization of the SHT

Extensive pre-heating characterization efforts were carried out in the SHT block to obtain site-specific thermal, mechanical, and hydrological rock properties. These site-specific data consist of laboratory measurements of grain density, matrix porosity, liquid saturation, thermal conductivity at different liquid saturation, heat capacity and thermal expansion coefficients (Tsang et al., 1996; Wang et al., 1997; SNL, 1996; CRWMS M&O 1997). Other than these site specific data, numerous laboratory measurements of ambient and thermal matrix properties were also available from borehole cores taken from the same hydrogeological unit as the SHT (Flint, 1996; Brodsky et al., 1997). Compared to the matrix, fracture properties were not well constrained by data from laboratory experiments due to scarcity of data; yet fracture permeability is one of the key parameters affecting thermal-hydrological behavior in the SHT, as the redistribution of moisture occurs primarily by vapor transport in the fractures. Therefore, a detailed field characterization by air permeability tests was carried out in the SHT block to determine the *in situ* fracture permeability prior to turning on the heater. As the fractures are essentially dry at ambient state, the rock permeability to air can approximately represent the saturated permeability of the fracture network, assuming that permeability to the gas phase and permeability to the water phase are similar.

Field Characterization of the SHT by Air Injection Tests

Air injection tests for the SHT area (Tsang et al., 1996) were performed after all the boreholes had been drilled and logged by video, and prior to the holes being installed with instrumentation

for monitoring the heater test proper. To prevent the boreholes from pneumatically communicating with the drifts, inflatable packers were fabricated and installed near the collar in every borehole numbered from 1 through 31. A typical test consisted of air injection in one chosen borehole at constant mass flux maintained by mass flow controllers. Pressure responses in this and all other boreholes were monitored continuously for about 20 to 30 minutes after steady state was reached, which was typically within minutes. Then air injection was terminated. Again, the steady-state pressure responses were obtained and recorded within about 15 minutes after the termination of air injection. The pressure response in the injection borehole itself is used to calculate the local permeability, averaged over the packed-off zone, L , specific to the injection hole. The interference pressure responses in all other boreholes yield information on the connectivity of pneumatic pathways between these observation holes and the injection hole.

Local Air Permeability Estimation

Local permeability in the injection borehole was estimated from the steady state pressure response to the air injection test. The analytical solution for the steady state pressure response of a constant flow rate injection in a finite line source is as follows:

$$k = \frac{P_{SC} Q_{SC} \mu \ln \frac{L}{r_w} T_f}{\pi L (P_2^2 - P_1^2) \gamma_{SC}} \quad (1)$$

For the meaning of notation, please see the nomenclature list. Equation (1) has been used by both LeCain (1995) and Guzman et al. (1996) for the analysis of single hole injection tests in fractured tuff at Apache Leap Research Site, Arizona. It was adapted from the steady state analytical solution for ellipsoidal flow of incompressible fluid from a finite line source (Hvorslev, 1951) in an infinite medium ($L/r_w \gg 1$). The derivation of Equation (1) requires the assumption that air is the only mobile phase within the rock near the test interval, and that it obeys the ideal gas law so that its compressibility is inversely proportional to pressure. Equation (1) has its origin in well test analysis for a homogeneous porous medium. The welded tuff of the single heater test block is a fractured medium and is most likely not well represented conceptually by a homogeneous porous medium. Furthermore, the proximity of the drifts implies that the finite line source is not in an infinite medium. Nevertheless, Equation (1) is valuable as a simple tool of choice to obtain

an order-of-magnitude estimate of the average permeability values around each borehole, thus providing an initial idea of the spatial variability of fracture permeability in the test block.

The permeability values as estimated from Equation (1) for injection tests performed in 21 boreholes in the SHT block are shown in Figure 3. The boreholes are designated by their collar locations on respective drift walls as shown in Figure 1b. These average permeability values are derived from borehole packed-off zones of lengths typically from 3 to 7 meters. Since the single heater block resides in the densely fractured Topopah Spring middle non-lithophysal stratigraphic unit, the spatial variability of the local permeability is expected to be large. Indeed, in the 21 boreholes that were tested, the estimated local permeability shown in Figure 2 ranges over three orders of magnitude, from a few milli-darcies to a few darcies. These values are on the same order of magnitude as those obtained from surface-based vertical boreholes at the SHT stratigraphic unit over zones of 2-3 m length (Rousseau, 1996; LeCain, 1997). Since borehole videos indicate differing degrees of fracturing in localized zones within each borehole, one would expect the permeability within each borehole to vary from one localized zone to another. This is confirmed by results of air injection tests performed in consecutive intervals of 0.61 m separated by a movable straddle packer string in Borehole 6. Indeed, the permeability values of the 18 consecutive zones in the same borehole again span a range of three orders of magnitude. Due to a time constraint requiring all characterization effort to be completed within a two-week period before permanent installation of the SHT, the detailed small scale characterization by straddle packer was not duplicated for other holes. The median air permeability value for all the single borehole and straddled sections tested is $5.85 \times 10^{-14} \text{ m}^2$.

Interference Pressure Responses

A typical set of air injection test data is shown in Figure 4 for air injection into a 4.9-m zone in Borehole 7. The horizontal axis denotes time, the right vertical axis denotes injection flow rate in standard liters per minute (SLPM), and the left axis denotes the pressure increase from ambient, ΔP , in kPa. The legend on the graph denotes all boreholes in which pressure response is monitored. The figure shows that the maximum pressure increase occurs in the injection hole. The pressures in the majority of the boreholes rise and fall in response to the constant-flow air injection in Borehole 7, though the magnitude of pressure response is smaller in holes other than the injection hole. The behavior displayed in Figure 4 is typical of that in all the boreholes tested.

The interference pressure data demonstrate that on the scale of one to ten meters, the fractures are well connected, and that the gas flow in the fractures resembles more that of flow through a heterogeneous continuum than flow through a discrete fracture network.

Further study of the cross-hole interference pressure responses of the air injection tests uncovers the presence of a high-permeability direct flow path from Borehole 11 to Boreholes 7, 6, and 12. Here, the magnitudes of pressure rise in the distant monitoring holes are similar to that in the injection hole. An examination of the borehole video logs show discrete zones of open, unfilled fractures in these holes lying in a common vertical plane oriented N22°E. Fracture mapping in the thermal alcove (CRWMS M&O, 1996) shows that there is indeed one subvertical joint set with that value of strike azimuth and having a length of three to four meters.

4. Modeling Approach

Conceptual Model and Input Parameters

Modeling of the SHT was carried out using the numerical simulator TOUGH2 (Pruess, 1987; 1991) for simulating multi-dimensional coupled transport of water, vapor, air, and heat in heterogeneous porous and fractured media. TOUGH2 accounts for the movement of gaseous and liquid phases (under pressure, viscous, and gravity forces according to Darcy's law, with interference between the phases represented by relative permeability functions); transport of latent and sensible heat; and phase transitions between liquid and vapor. Mass- and energy-balance equations are written in integral form for an irregular flow domain in one-, two-, or three-dimensions. The physical processes of capillary suction and adsorption in the liquid phase, binary diffusion in the gas phase, thermal expansion and porosity changes in the rock mass in response to pore pressure, as well as the effect of vapor pressure lowering due to capillary and phase adsorption effects are all included in the simulator. Thermal conductivity is assumed to be saturation dependent, having a functional dependence on a "dry" and "wet" thermal conductivity. Key equations for these physical processes are summarized in Appendix A: namely, matrix and fracture characteristic curves defined by the air entry parameter $1/\alpha$ and pore size distribution

coefficient β ; the gas phase diffusion and vapor pressure lowering formulation; and the saturation dependence of the thermal conductivity,

For the thermal-hydrological simulations, the welded tuff in which the SHT resides is conceptualized as a dual continuum, composed of the matrix continuum with very low permeability, and the fracture continuum with permeability orders of magnitude higher. Laboratory measurements of hydrological properties on cores were assigned to the matrix continuum. Where matrix data specific to the SHT were not available (e.g., permeability, capillary pressure, and relative permeability characteristic curve parameters α , β), measured parameter values from other locations in the respective stratigraphic unit were employed. The assignment of fracture permeability values was based on the field air-permeability measurements presented above. Since the interference pressure data indicate that the fractures are well connected, the fracture continuum was assigned a background permeability of $5.8 \times 10^{-14} \text{ m}^2$, the median of all measured values. And since the combined data of fracture mapping, borehole video logs, and air injection interference tests indicate the presence of a high permeability feature, about 4 m in extent, our conceptual model also included a high permeability ($5.2 \times 10^{-12} \text{ m}^2$) zone to the south-west of the heater, superposed on the uniform background permeability. A more detailed spatial heterogeneous structure for the background fracture permeability, which matches all the measured interference data, is now being constructed, but not yet included in the simulations presented in this paper. Since no measurements are available for other fracture properties (such as porosity or characteristic curve parameters), we base our choice on estimates derived from calibration efforts for the Yucca Mountain Site Scale Model (Bodvarsson et al., 1997).

Other than assigning appropriate material properties to the fracture and matrix continua, it is also important to account for the interaction between the matrix and fractures. In our dual-continuum approach, the entire geometric matrix-fracture interface, estimated from fracture mapping along the ESF tunnel walls (Sonnenthal et al., 1997), is assumed to participate in the matrix-fracture coupling. We do not account for a possible reduction of the matrix-fracture interaction—arising from fracture coating, flow channeling in fractures, and other factors—which can impact the simulated thermal-hydrological response of the SHT. For large 3-D problems, the dual continuum formulation can be extremely computationally intensive, and a conceptual simplification is often employed that treats the matrix and the fractures as one effective continuum (Pruess et al., 1990).

This concept involves the crucial assumption that a capillary pressure equilibrium between the fractures and matrix is maintained at all times. As a result, gravity driven liquid flow in the fractures tends to be underestimated, since vapor condensing on the fracture walls is assumed to be readily imbibed into the matrix pores because of the equilibrium assumption. As the main differences between the dual permeability and the effective continuum conceptual models are hydrodynamic in nature, they are not captured by passive temperature monitoring data. However, the different drainage behavior associated with the two conceptual models may give rise to different signatures in the active tests that specifically probe the moisture redistribution during the SHT. Therefore the thermal-hydrological response of the SHT assuming an effective continuum conceptual model, in addition to the dual permeability model, will be presented in this paper for comparison.

The hydrological and thermal input parameters used in the numerical simulations for the SHT are presented in Table 1. Note that isotropy is assumed for all properties. Possible chemical or mechanical alterations in response to the heating are not included in our model. However, the thermal-mechanical and the thermal-chemical coupled processes have been considered and analyzed by other SHT thermal testing team members (Sobolik et al., 1996; CRWMS M&O, 1997; Glassley, 1997; SNL 1997). We assign rock properties for all boreholes except for the heater hole, thus making the implicit assumption that wiring, grouting, and instrumentation in the test block do not affect the thermal-hydrological behavior.

Grid Design, Boundary and Initial Conditions

The computational domain for the thermal-hydrological simulations includes the entire 3-D test block plus significant rock volumes added in all directions to guarantee a proper definition of boundary conditions. The top and bottom boundaries of the test block are 14 m each from the heater hole; they are sufficiently far from the heater to represent infinite boundary conditions (constant pressure, temperature and liquid saturation for the top, and free drainage conditions for the bottom). North, south and west boundaries are each extended to the outer walls of the alcoves and treated as no-flow boundaries for heat, liquid and gas. The alcove geometry is explicitly modeled. The three alcove walls surrounding the test block are insulated with a low thermal conductivity material. Though these walls are explicitly modeled as thermal barriers, they are

assumed to be open for moisture to escape from the test block in the form of both liquid water and vapor. The floor and the ceiling of the alcoves are not insulated; thus they are designated boundaries with constant state variables.

Figure 5 shows the discretization designed for the SHT; Figure 5a presents a XZ cross section chosen perpendicular to the heater centerline, Figure 5b gives a plane view intersecting the heater hole. The 3-D grid comprises about 30,000 gridblocks and more than 100,000 connections between them. The origin of the computation coordinates is at the collar of Heater Hole 1. The design of the grid is to achieve a proper balance between desired numerical accuracy and computational time, both of which are controlled by the total number of gridblocks. Fine gridding and radial symmetry is maintained around the heater hole to be compatible with sharp gradients of temperature, saturation and pressure. With increasing distance from the heater, the grid is converted gradually to cartesian coordinates in order to better represent the boundaries of the drift and alcove walls. The size of the gridblocks starts as small as 0.02 m at the heater hole and increases up to 0.5 m at a distance of 5 m. Figure 5b indicates the location of the localized subvertical fracture zone with higher permeability.

The initial conditions for the model domain were chosen as 87.0 kPa for gas pressure, 25 °C for temperature, and 0.92 for matrix saturation, as given by pre-heating characterization of the SHT. For lack of data, the corresponding fracture liquid saturation, 0.052, was calculated from the matrix saturation assuming a capillary pressure equilibrium between matrix and fractures at ambient state. No geothermal gradient was assigned because of the small vertical extension of the SHT. A typical geothermal gradient of 0.02 °C/m would only give a temperature difference of 0.56 degrees between the top and the bottom model boundary, which is negligibly small compared to the temperature perturbation generated by the heater.

5. Simulation Results and Comparison with Measured Data

Introducing a heat source in the unsaturated fractured tuff gives rise to strong two-phase flow effects, contributing to heat transfer in the near field environment. Although heat conduction is the dominant heat transport process, heat transfer due to gas or liquid flow can influence the

spatial or temporal distribution of temperatures, evidenced in often subtle, sometimes strong temperature “plateaus” near the nominal boiling point. The relative importance of convective heat transfer is related to the respective hydrological properties of the fractures and the matrix, and to the temporal and spatial scale of the heat perturbation in a complex, non-linear manner. Careful analysis of the SHT temperature data, from both active and passive testing, can help to constrain hydrological properties of the fractured rock mass.

Temperature Data - Dual Permeability Conceptualization

The continuous passive monitoring data of the SHT in multiple locations enable the display of data either as snapshot or as time evolution at a particular spatial location. Figure 6 shows a snapshot (1/2 month after heating initiated) of temperature data from all the boreholes with temperature sensors. The temperature is displayed as a function of radial distance from the Heater Hole 1. For each of the boreholes parallel to Heater Hole 1, multiple sensors at different locations along the borehole register different temperatures due to the finite length of the heater. The temperatures close to the heater are already well above the nominal boiling point at 1/2 month of heating, showing that vapor-liquid counterflow is not strong enough to maintain a heat pipe condition at that region.

Figures 7 and 8 show respectively the comparison of the measured and simulated results for the subset of temperature data measured close to the mid-plane of the heater, at 3 months and 9 months of heating. The simulations were carried out with the dual permeability conceptualization. Simulated matrix and fracture temperatures are similar except near the nominal boiling point, where the fracture temperature slope shows a plateau, indicative of substantial heat transfer contributions from vapor-liquid counterflow in the fractures. The two-phase heat pipe region centers around 0.8 m radial distance from the heater at 3 months of heating, and moves out to about 1.2 m at the end of 9 months of heating. It is unfortunate that there is a lack of temperature sensors at these distances. Nevertheless, the simulated temperatures compare favorably with the measured data, although overpredicting somewhat in the region between radial distance of 1.2 m to 3.5 m.

Figure 9 presents the time evolution of temperatures over the 9 months of heating for the sensor at $y = 4.5$ m, given for each of the boreholes parallel to Heater Hole 1. The down spikes in the measured data register incidences of power outage. The majority of the instrument boreholes were grouted, with the exception of Boreholes 2, 3, and 4, which are open to allow for mechanical displacement measurements. Thus, the sensors in grouted holes are expected to represent the rock matrix temperatures, and should therefore be compared with the simulated temperatures of the matrix continuum. The temperature in open holes may be somewhat modified by convective heat transfer within the boreholes. Analysis of all temperature data from sensors registering temperatures above 100 °C shows generally very subtle, if any, heat pipe effects, indicating that the dominant heat transfer mechanism operating in the SHT is heat conduction.

Comparison between the measured data and the simulated matrix temperatures shows good overall agreement. The overprediction of temperature in Borehole 11 may be due to the model approximation of a uniform background fracture continuum permeability of $5.8 \times 10^{-14} \text{ m}^2$, which is two orders of magnitude smaller than that measured specifically for Borehole 11 from air permeability testing (Figure 4). A larger fracture permeability will promote heat transfer by convection resulting in lower temperature. It is not known whether the spatial heterogeneity of fracture permeability also accounts for the discrepancy between simulations and measured data in Borehole 8 since no air injection tests were carried out for Hole 8 in the pre-heating characterization effort. Note that the simulated fracture temperatures display a more prominent heat pipe effect for a longer duration than the simulated matrix temperatures and the monitored data. Apparently, liquid flow in the matrix is too slow to allow for a significant vapor-liquid counterflow signal in the temperature evolution.

To evaluate the effect of thermal-hydrological coupling in the SHT, additional simulations were carried out where fluid movement was suppressed and heat transfer limited to conduction alone. Figures 10 and 11 show the comparison of the conduction-only simulations with the monitored data at 9 months of heating, for the thermal conductivity values of 1.67 W/(m °K) and 2.0 W/(m °K) respectively. These conductivity values bracket the range of laboratory-measured values for the SHT samples, which range from dry to fully saturated welded tuff (CRWMS M&O, 1997). A comparison of Figures 10 and 11 with Figure 9 where the thermal-hydrological coupling is

incorporated show clearly that, though conduction is the dominant heat transfer mode, the convective heat transport due to hydrological coupling serves to lower the temperature of the rock mass, bringing the calculation to a better match with the temperature data.

Liquid Saturation - Dual Permeability Conceptualization

Figures 12 and 13 show the simulated liquid saturation and liquid flux at 3 months for the fracture and matrix continuum respectively, in a close-up view of the mid-plane of the heater at $y = 4.5$ m. For both the fracture and matrix continua, drying occurs up to a radial distance of about 1 m from the heater, beyond which is the condensation zone where liquid saturation is higher than that at ambient conditions. In the fracture continuum, the condensation zone is very extended, showing a significant saturation increase (from the initial saturation 0.052) indicative of strong vapor fluxes away from the boiling zone. Downward drainage flux is appreciable below the heater, as the capillary pressure gradient in the fractures is overcome by gravity. In the matrix, the saturation build-up in the condensation zone is less apparent and less extended than in the fractures. Apparently, the vapor condenses and is being mobilized in the fractures faster than it is being drawn into the matrix, so that only a small fraction of condensate imbibes into the rock pores. This leads to a condition of disequilibrium between fractures and matrix. The rock matrix is drier above the heater than below, not because of gravity-driven liquid flux in the matrix, but from the downward drainage in the fractures and subsequent imbibition into the matrix pores. Note that the thermally induced liquid fluxes are orders of magnitude larger than the ambient percolation flux at Yucca Mountain of at most tens of mm per year (Flint et al., 1997).

The redistribution of the moisture content described by the numerical model is consistent with the results of active testing by neutron logging, cross-hole radar tomography, and air permeability tests carried out both prior to and periodically during the SHT. Active tests were carried out in Boreholes 15, 17, 22, 23 (see Figure 1b) for neutron logging and radar tomography, and Boreholes 16 and 18 for air permeability. All these boreholes are orthogonal to the heater centerline located in the mid-plane at approximately $y = 4.5$ m. While neutron logging and radar tomography data probe the change in water content in the matrix (which accounts for most of the porosity), air permeability tests give information on liquid saturation changes in the fractures.

Ground penetrating radar surveys were carried out before the heater turn-on, and then at 4.5 months and 6.5 months of heating (Peterson and Williams, 1997). The radar velocity fields produced from tomographic inversion show that at 4.5 months after heating, there is an increase in velocity around the heater, while decrease in velocity occurs about 1 m away from the heater, toward the alcove walls. The tomogram at 6.5 months shows further velocity increases near the heater, but velocity in the areas beyond 1 m radius does not decrease any more. These radar velocity changes are indicative of a decrease in liquid saturation near the heater, and an increase in liquid saturation further away from the heater. This is consistent with the thermal-hydrological conditions of a drying zone around the heat source and a condensation zone commencing about 1 m away, as predicted by the simulations (Figure 12). That the velocity at 4.5 months and 6.5 months of heating shows similar radar velocity decrease indicates that there is little change in the moisture content of the condensation zone after 4.5 months of heating, again consistent with simulated results showing that most of the liquid saturation build-up occurs in the first 3 months of heating. Electrical resistivity tomography and neutron logging data also show drying around the heater and build-up of moisture content outside the drying zone (CRWMS M&O, 1997).

The formation of an incised saturation zone during the first few months of heating is also corroborated by the air permeability data. Constant flowrate air injection tests were carried out in different zones isolated by four high temperature packers in Boreholes 16 and 18. Then as liquid saturation in the fractures increases in the condensation zones, one would expect that the apparent permeability for air should decrease. Indeed, the estimated air permeability values in the zone between 1 m to 3 m from the heater (which corresponds to the simulated condensation zone in the fracture continuum) decreased by a factor of 4 in Borehole 16 and a factor of 2 in Borehole 18, at 3 months of heating, from their pre-heat values (Freifeld and Tsang, 1997; CRWMS M&O, 1997). On the other hand, permeability values in zones with radial distance larger than 3 m featured little change from their preheat values. Furthermore, little change was observed in permeability values from 3 months onwards through the heating phase, regardless of whether the observation was within or outside of the simulated condensation zone.

Liquid Saturation and Temperature - Effective Continuum Conceptualization

In this section, we analyze the saturation and fluxes from an alternative simulation study based on an effective continuum model, where matrix and fractures are constrained to be in thermodynamic equilibrium at all times. Results for fracture and matrix saturation and liquid fluxes are presented in Figures 14 and 15, respectively. These figures are quite different from those of the dual permeability model in Figures 12 and 13, in that there appears to be a symmetry of the saturation contours about the heater horizon $z = 0$ m, and there is the absence of gravity driven drainage flux in the fractures. Furthermore, the fracture saturation buildup in the condensation zone is much smaller and less extended in the effective continuum model compared to the dual continuum model, whereas the matrix saturation is much higher. The reason for these very obvious differences is the assumption of equilibrium between fractures and matrix: As soon as the vapor condenses in the fractures, it is being imbibed into the matrix. The actual transient nature of the processes cannot be captured by the effective continuum model. Consequently, the fracture saturation builds up only marginally, and little if any flux is seen in the fracture continuum. In the matrix, however, a well-defined symmetric zone of condensation is formed between a radial distance of 0.8 m to 3 m from the heater, allowing capillary-driven liquid reflux toward the boiling zone.

While the flux dynamics are very different in the effective continuum and dual permeability models, the two models are not expected to give vastly different thermal behavior. Indeed, Figures 16 and 17, which show the temperature predictions from the effective continuum model for 3 months and 9 months, are similar to those from the dual permeability model (Figures 7 and 8), but have a slightly poorer match for temperature above boiling at small radial distances. The effective continuum results tend to underpredict the monitored temperature. This is also demonstrated in Figure 18, where the temperature time evolution of all boreholes parallel to Heater Hole 1 is shown, and which is to be compared to Figure 9 which describes the dual permeability results. Both model concepts show identical results as long as the temperatures stay well below 100 °C; however, a more distinct heat pipe signature develops in the temperature evolution from the effective continuum model, and the temperatures above the nominal boiling point are about 5 °C lower than temperatures from the dual continuum model. The suppression of temperature in the effective continuum results is a result of the strong capillary pressure driven

liquid flow (in the matrix) back to the heater, which in turn increases convective transport of heat away from the heater.

Since the differences between the two model concepts are rather subtle, and since the conceptualization of the fracture-matrix interaction is only one of the many factors that can give rise to different temperature predictions, we are not able to discriminate the dual permeability and the effective continuum models by the measured temperature alone. As for the active testing to monitor the redistribution of moisture, both electrical resistivity tomography (CRWMS M&O, 1997) and cross-hole radar tomography data seem to indicate that the tuff formation is slightly wetter below the heater than above the heater, thus favoring the dual permeability formulation. In the near future, additional data will become available for the cooling phase of the SHT. These data may provide further evidence for confirming one or the other model concept, as rewetting of the dry-out zones around the heater is significantly different for the two conceptual models. In the dual permeability model, most of the condensate drains away from the SHT and is not available for rewetting. The effective continuum model, on the other hand, allows for faster rewetting since the majority of the mobilized water is being stored in the matrix pores of the condensation zone close to the dried-out areas around the heater.

Sensitivity Studies

The good agreement between the measured data and the simulated results as shown in previous sections indicates that the thermal-hydrological response of the SHT in the 9 months of heating is well represented by the coupled thermal-hydrological numerical models. While heat conduction accounts for most of the temperature rise, the effects of thermal-hydrological coupling cannot be ignored in the interpretation of the measured data. In particular, the choice of different parameter values assigned to the hydrological properties can play a significant role in affecting the simulation results. Since the spatial heterogeneity and uncertainty of the hydrological properties, particularly for the fractures, is large, we shall present below the sensitivity of the simulated temperatures to some key properties of the fractured rock: continuum permeability and air entry pressure values for the matrix and fracture continua. Insight from these studies can serve to constrain these hydrological properties. The sensitivity study is performed using a dual-permeability formulation for the vertical mid-plane of the heater, at $y = 4.5$ m. The base case

referred to in the following corresponds to the set of parameters employed in the 3-D simulations of the SHT test as presented in the last section above. From the base case, only one parameter at a time is varied; while all other parameters are kept constant.

Figure 19 shows the temperature history in the matrix at a radial distance of 0.67 m from the heater, for the base-case matrix permeability and for cases where the matrix permeability is increased and decreased by one order of magnitude. Note that the decrease of matrix permeability has little effect, but the increase of matrix permeability results in a large suppression of temperature. The latter arises from (1) increased imbibition of condensate from the fractures into the matrix, and (2) increased liquid flow back to the heater area through the matrix continuum. On the other hand, the lowering of matrix permeability from the base case has negligible effect because the base case value is already low enough that only minor imbibition and liquid reflux is present.

Figure 20 shows the temperature history for the base case, and for cases where the fracture permeability is increased and decreased by one order of magnitude. A higher fracture permeability promotes increased convective heat transport by removal of vapor from the heater area, giving rise to lower temperatures. Assigning a lower permeability to the fractures does the reverse, resulting in higher temperature. Overall, the temperature evolution is less sensitive to a one-order-of magnitude change in the fracture permeability than to a one order of magnitude change in the matrix permeability

Figure 21 shows the sensitivity of the temperature history to the matrix characteristic curve parameter α (see Equation A1)—which is a measure of the inverse air entry pressure—by comparing to cases where α is decreased and increased by one order of magnitude relative to the base case. The smaller α implies a stronger capillary suction in the matrix, which tends to promote imbibition of condensate into the matrix. Thus, more water is available in the matrix to be driven toward the heater area, resulting in increased convective heat transfer and lowering of the temperature. A larger α has the opposite effect; however, a one order of magnitude increase in α has a rather small impact on the temperatures. As discussed earlier, the base-case matrix properties already gives rise to little matrix imbibition and liquid reflux, so the effect of a further increase in α is negligible.

Figure 22 shows the sensitivity to fracture characteristic curve parameter α , by comparing to cases where the fracture α is increased and decreased by one order of magnitude relative to the base case. The effect on the temperature is similar to that of the matrix parameter α , in that a smaller α promotes lower temperatures, and a higher α promotes an increase in temperature. However, now the different capillary behavior of the fracture continuum enhances or limits liquid reflux toward the heated area within the fractures, while a change in matrix α in Figure 21 affects imbibition and reflux in the matrix. Ultimately, if the fracture α parameter is decreased further, capillary forces in the fractures would dominate gravity forces, altogether suppressing downward drainage away from the heater.

The examples shown in Figures 19 through 22 demonstrate that one order of magnitude variation in some of the key parameters can significantly alter the simulated temperature of the SHT. One order of magnitude variation is well within the limit of the spatial heterogeneity and uncertainty of the hydrological properties within the fractured welded tuff. In particular, one can conclude from the above analysis that property sets with higher matrix permeability, smaller matrix α , or smaller fracture α than the 3-D base case values are not likely to represent the SHT thermal-hydrological situation. All these cases overestimate vapor-liquid counterflow and underestimate the observed temperatures. For the other cases, changes in temperature with parameter variation are rather subtle and well within the error margin between simulated and measured temperatures, thus offering no help in property constraints.

Additional sensitivity studies have shown that varying the other characteristic curve parameter β (see Equation A1), which is related to the variability of fracture apertures, hardly changes the simulated temperature. Varying thermal conductivity parameters C_{dry} and C_{wet} within the range allowed by the laboratory measurements produces qualitatively little change in the simulated temperature. We also studied the sensitivity of SHT temperatures to the ambient percolation flux through the mountain. Varying the percolation flux from 0.1 mm/yr to about 20 mm/yr changes the initial fracture saturation in the SHT block, but gives rise to an almost identical temperature response during heating. This is because reasonable values of percolation are negligibly small compared to the thermally induced fluxes. Thus, the SHT results cannot help to put constraints on percolation flux estimates at Yucca Mountain.

Findings from the above sensitivity studies are specific to a small scale experiment. The sensitivities identified for the SHT may not hold for the larger Drift Scale Test, the repository, or for different heater geometry. The thermal-hydrological behavior is controlled by the relative strengths and time constants of multiple processes: matrix imbibition of condensate, capillary-driven flow, and gravity drainage in the matrix and fractures. In the SHT, the impact of the thermal perturbation is localized and intense, in that vaporization and condensation per rock volume and time is very large. The localized and intense perturbation may have accentuated the differences in model prediction of thermal-hydrological behavior from different conceptual models and hydrological properties.

6. Summary and Conclusions

The Single Heater Test (SHT) is one of two *in-situ* thermal tests included in the site characterization program for the potential underground nuclear waste repository at Yucca Mountain. The heating phase of the SHT started in August 1996 and was completed in May 1997 after 9 months of heating. The coupled thermal-hydrological processes in the fractured rock mass around the heater were monitored by numerous sensors for thermal, hydrological, mechanical, and chemical data. In addition to passive monitoring, active testing of the rock mass moisture content was performed using geophysical methods and air injection testing. The extensive data available from this test give a unique opportunity to improve our understanding of the thermal-hydrological situation in the natural setting of the repository rocks.

In the present paper, we have simulated the thermal-hydrological processes in the SHT using a 3-D numerical model of the fractured tuff in the heater vicinity, and compared the simulation results with the monitored data. As much as possible, site-specific thermal and hydrological data have been used as input parameters for the SHT model. The good agreement between the temperature data and simulated results indicates that the thermal-hydrological responses of the SHT in the 9 months of heating are well represented by the coupled thermal-hydrological numerical model. Fine tuning the thermal conductivity and heat capacity values can improve further the fit between modeled results and data. On the other hand, the varying degree of discrepancy between simulations and measurement in different boreholes may in part be attributed to spatial

heterogeneity. An analysis of the data by taking account of the heterogeneity structure of the fracture permeability, based on matching all pre-heat interference pressure data from air injection tests, is now underway.

Our interpretation of the SHT data through numerical modeling shows that while heat conduction accounts for most of the temperature rise, the contribution from thermal-hydrological coupling is important. If hydrological effects were ignored and only heat conduction was simulated using site-specific measured thermal conductivity values, the model result would give a rather poor fit to the temperature data. Overall, the signature of vapor and liquid counter flow is very subtle in the temperature data. Short duration heat pipe is often evidenced by only a hint of inflection of slope at nominal boiling temperature in the time evolution graphs. The data therefore indicate that the hydrological properties of the matrix and fractures at the SHT are such that they do not promote appreciable liquid reflux to the heater from the condensed vapor during the heating phase. A sensitivity study was carried out to gain a better understanding of how the coupled thermal-hydrological processes in the repository formation are affected by matrix and fracture properties, and by the geometry and scale of the test. Results of the sensitivity study provide constraints on some hydrological parameters of the fractured rock mass, which are very uncertain; but cannot discriminate other parameters, such as the ambient percolation flux.

Aside from the continuous monitoring data, the change of moisture content in the rock mass was probed by periodic active testing. The cross-hole radar tomography and air permeability tests both indicate a dry-out zone of about 1 m around the heater hole and a condensation zone of increased liquid saturation outside of the dry-out zone. These active testing data, including the electrical resistivity tomography and neutron logging data, all indicate that the moisture content is larger below than above the heater, suggesting gravity drainage is present during the heating phase. Our numerical simulations show that gravity drainage occurs in the dual-permeability conceptual model, but is absent in the effective-continuum model, where matrix and fractures are required to be in thermodynamic equilibrium at all times. The cooling data should further discriminate the alternative conceptual model since the drained water would not be available for rewetting of the dried-out regions close to the heater.

The *in situ* SHT has greatly increased our understanding of the coupled processes in fractured, porous rock. It has also served its function well as a shakedown test for the longer-duration and larger-scale Drift Scale Test. We have gained invaluable insight in testing methods, modeling, and data interpretation strategies from the conducting and the analysis of the SHT.

Nomenclature

C	Thermal conductivity (W/m °K)
C_{wet}	Thermal conductivity parameter for saturated rock (W/m °K)
C_{dry}	Thermal conductivity parameter for dry rock (W/m °K)
D_{va}	Diffusion coefficient for the vapor-air mixture in a porous medium (m ² /s)
D_{va}^o	Diffusion coefficient at standard conditions (m ² /s)
f_{vpL}	Vapor pressure lowering factor
k	Permeability (m ²)
k_m	Matrix continuum permeability (m ²)
k_f	Fracture continuum permeability (m ²)
$k_{r,l}$	Liquid relative permeability
$k_{r,g}$	Gas relative permeability
$k_{r,m}$	Matrix relative permeability
$k_{r,f}$	Fracture relative permeability
k_b	Effective continuum permeability of fluid phase b (m ²)
L	Length of air injection zones (m)
m_l	Molecular weight of liquid
$m = 1 - 1/\beta$	van Genuchten parameter for characteristic curves
P_1, P_2	Initial pressure and final steady state pressure for air injection tests (Pa)
P_{sc}	Pressure at standard conditions, 1.013×10^5 Pa
P_{cap}	Capillary pressure (Pa)
P_v	Vapor pressure (Pa)
P_{sat}	Saturated vapor pressure (Pa)
R	Universal gas constant
Q_{sc}	Flowrate at standard conditions in air injection tests (m ³ /s)
r_w	Radius of boreholes (m)
S_b	Effective continuum saturation
$S_{b,m}$	Effective continuum phase saturation in matrix
$S_{b,f}$	Effective continuum phase saturation in fracture
S_g	Gas saturation
$S_{l,eff}$	Liquid effective saturation
S_l	Liquid saturation

S_r	Residual liquid saturation
T	Temperature (°C)
T_f	Temperature of formation in air injection tests (° K)
T_{SC}	Temperature at standard conditions (273.15 °K)
α	van Genuchten parameter for characteristic curves, (Pa) ⁻¹ , $1/\alpha$ is the air entry pressure
β	van Genuchten parameter, pore size distribution coefficient
ϕ	Porosity
ϕ_m	Matrix porosity
ϕ_f	Fracture porosity
λ	Brooks-Corey relative permeability curve parameter
μ	Dynamic viscosity of air (Pa-s), 1.81×10^{-5} at 20 °C
θ	Temperature dependence factor for vapor diffusion
ρ_l	Liquid density (kg/m ³)
τ	Tortuosity

Appendix

Some key equations for the processes included in the numerical simulations are as follows. Matrix and fracture continua are given the same functional dependence in the characteristic curves. The capillary suction and the relative permeability for liquid have the van Genuchten functional forms (Van Genuchten, 1980; Mualem, 1976):

$$\begin{aligned}
 P_{cap} &= -\frac{1}{\alpha} \left\{ \left(S_{l,eff} \right)^{-\frac{1}{m}} - 1 \right\}^{\frac{1}{\beta}} \\
 k_{r,l} &= \left(S_{l,eff} \right)^{\frac{1}{2}} \left\{ 1 - \left(1 - \left(S_{l,eff} \right)^{\frac{1}{m}} \right)^m \right\}^2 \\
 S_{l,eff} &= \frac{(S_l - S_r)}{(S_s - S_r)} .
 \end{aligned} \tag{A1}$$

For the relative permeability to gas we do not apply the common formulation as $(1 - k_{r,l})$ because the van Genuchten functional dependence has an extremely steep slope for liquid relative permeability near full liquid saturation, giving rise to unrealistically large gas relative

permeability values even for very small gas saturation. Therefore, we choose the Brooks-Corey formulation

$$k_{r,g} = (1 - S_{l,eff})^2 \left(1 - S_{l,eff}^{\frac{2+\lambda}{\lambda}} \right) \quad (A2)$$

In the effective-continuum approximation, the fracture and matrix continua are characterized by the same temperature and pressure, where the effective continuum saturation S_b is given by:

$$S_b = \frac{S_{b,m}\phi_m + S_{b,f}\phi_f}{\phi_m + \phi_f} \quad (A3)$$

and the effective-continuum phase permeability k_b is :

$$k_b = k_m k_{r,m} + k_f k_{r,f} \quad (A4)$$

The diffusion coefficient D_{va} for the vapor-air mixture in a porous medium is given by Vargaftik, (1975); and Walker et al. (1981),

$$D_{va} = \tau \phi S_g D_{va}^o \frac{P_{SC}}{P} \left[\frac{T}{T_{SC}} \right]^0. \quad (A5)$$

The vapor pressure lowering effect is represented by Kelvin's equation (Edlefsen and Anderson, 1943)

$$f_{VPL} = \frac{P_v(T, S_l)}{P_{sat}(T)} = \exp \left(\frac{m_l P_{cap}(S_l)}{\rho_l R(T + 273.15)} \right) \quad (A6)$$

where f_{VPL} , the vapor pressure lowering factor is identical to the definition of relative humidity. The readings in the relative humidity sensor can serve to monitor the evolution of the dry-out region where the capillary pressure P_{cap} attains a very strong negative value.

The saturation dependence of the thermal conductivity is given by:

$$C(S_l) = C_{dry} + (C_{wet} - C_{dry}) \sqrt{S_l} \quad (A7)$$

Acknowledgment

We thank Chin-Fu Tsang and Eric Sonnenthal for their review of the manuscript and comments for improvement. This work was supported by the Director, Office of Civilian Radioactive Waste Management, U.S. Department of Energy, through Memorandum Purchase Order EA9013MC5X between TRW Environmental Safety Systems. Inc. and the Ernest Orlando Lawrence Berkeley National Laboratory, under Contract No. DE-AC03-76SF00098.

Table 1. Hydrological and thermal input values

Parameter	Value	Comments
Matrix Porosity	0.11	Flint, 1996
Matrix Permeability	$4.0 \times 10^{-18} \text{ m}^2$	Flint, 1996
Matrix van Genuchten parameter α	$6.4 \times 10^{-7} \text{ Pa}^{-1}$	Flint, 1996
Matrix van Genuchten parameter $\beta = 1/(1-m)$	1.47	Flint, 1996
Brooks Corey parameter λ for gas phase permeability	2	
Matrix Residual Liquid Saturation	0.18	Flint, 1996
Matrix Grain Density	2540.0 kg/m^3	SHT laboratory measurements
Initial Matrix Liquid Saturation	0.92	SHT laboratory measurements
Fracture Porosity	0.000243	Bodvarsson et al., 1997.
Fracture Permeability (low permeability background)	$5.85 \times 10^{-14} \text{ m}^2$	SHT field measurements
Fracture Permeability (high-permeability feature)	$5.2 \times 10^{-12} \text{ m}^2$	SHT field measurements
Fracture van Genuchten α	$1.0 \times 10^{-3} \text{ Pa}^{-1}$	Bodvarsson et al., 1997.
Fracture van Genuchten β	1.47	Bodvarsson et al., 1997.
Fracture Residual Liquid Saturation	0.01	Bodvarsson et al., 1997.
Rock Mass Thermal Conductivity $C(S_l) = C_{dry} + (C_{wet} - C_{dry})\sqrt{S_l}$	$C_{dry} = 1.67 \text{ W/(m } ^\circ\text{K)}$ $C_{wet} = 2.0 \text{ W/(m } ^\circ\text{K)}$	SHT laboratory measurement.
Rock Mass Heat Capacity	$953.0 \text{ J/(kg } ^\circ\text{K)}$	Brodsky et al., 1997.
Heater Power (9-month average data)	3758 W	SHT heating phase data
Vapor Diffusion Coefficient D_{va}^0 Temperature dependence θ	$2.14 \times 10^{-5} \text{ m}^2/\text{s}$ 2.334	Pruess and Tsang, 1994
Fracture Spacing	0.53 m	Sonnenthal et al., 1997.

Figure Captions

- Figure 1a. Schematic of borehole layout in the SHT (3D perspective).
- Figure 1b. Borehole layout in the SHT (plan view and cross section).
- Figure 2. A schematic diagram of the coupled thermal-hydrological processes in the SHT.
- Figure 3. Local air permeability estimated from pre-heat air injection tests in 21 boreholes in the SHT block.
- Figure 4. Flow and interference pressure responses of a typical air injection test performed in the pre-heat characterization of fracture permeability.
- Figure 5. Numerical grids for simulation of the SHT.
- Figure 6. Temperature data from boreholes 2, 3, 4, 5, 8, 9, 10, 11, 12, 13, 14, 15, 16, 17, 18, 22, 23.
- Figure 7. Measured and simulated temperature at 3 months, for the dual permeability conceptual model, for temperature sensors in the center-plane of the SHT block at $y = 4.5$ m.
- Figure 8. Measured and simulated temperature at 9 months, for the dual permeability conceptual model, for temperature sensors in the center-plane of the SHT block at $y = 4.5$ m.
- Figure 9. Measured and simulated temperature history, with the dual permeability conceptual model, for all boreholes parallel to Heater Hole 1, for temperature sensors in the center-plane of the SHT block.
- Figure 10. Measured and simulated temperature at 9 months for heat-conduction-only model, for temperature sensors in center-plane of the SHT block. Heat conductivity is $1.67 \text{ W/(m}^\circ\text{K)}$.
- Figure 11. Measured and simulated temperature at 9 months for heat-conduction-only mode, for temperature sensors in center-plane of the SHT block. Heat conductivity is $2.0 \text{ W/(m}^\circ\text{K)}$.
- Figure 12. Fracture saturation and liquid flux at 3 months with the dual permeability conceptual model, shown for the center-plane of the SHT block. The xy-diagram shows distribution of saturation and flux along the z-axis at $x=0.0$ m. Positive flux values denote upward flow, negative flux values denote downward flow.
- Figure 13. Matrix saturation and liquid flux at 3 months with the dual permeability conceptual model, shown for the center-plane of the SHT block. The xy-diagram shows distribution of saturation and flux along the z-axis at $x=0.0$ m. Positive flux values denote upward flow, negative flux values denote downward flow.

Figure 14. Fracture saturation and liquid flux at 3 months for simulation with the effective continuum model, shown for the center-plane of the SHT block. The xy-diagram shows distribution of saturation and flux along the z-axis at $x=0.0$ m. Positive flux values denote upward flow, negative flux values denote downward flow.

Figure 15. Matrix saturation and liquid flux at 3 months for simulation with the effective continuum model, shown for the center-plane of the SHT block. The xy-diagram shows distribution of saturation and flux along the z-axis at $x=0.0$ m. Positive flux values denote upward flow, negative flux values denote downward flow.

Figure 16. Measured and simulated temperature at 3 months, for the effective continuum conceptual model, for temperature sensors in the center-plane of the SHT block at $y = 4.5$ m.

Figure 17. Measured and simulated temperature at 9 months, for the effective continuum conceptual model, for temperature sensors in the center-plane of the SHT block at $y = 4.5$ m.

Figure 18. Measured and simulated temperature history, with the effective continuum conceptual model, for all boreholes parallel to Heater Hole 1, for temperature sensors in the center-plane of the SHT block.

Figure 19. Sensitivity of temperature to matrix permeability, at a radial distance of 0.67 from the heater. Simulation is for the dual permeability conceptual model in a x-z vertical plane at $y = 4.5$ m.

Figure 20. Sensitivity of temperature to fracture permeability, at a radial distance of 0.67 m from the heater. Simulation is for the dual permeability conceptual model in a x-z vertical plane at $y = 4.5$ m.

Figure 21. Sensitivity of temperature to matrix α parameter, at a radial distance of 0.67 m from the heater. Simulation is for the dual permeability conceptual model in a x-z vertical plane at $y = 4.5$ m.

Figure 22. Sensitivity of temperature to fracture α parameter, at a radial distance of 0.67 m from the heater. Simulation is for the dual permeability conceptual model in a x-z vertical plane at $y = 4.5$ m.

References

- Birkholzer, J.T. and Y. W. Tsang, 1996. Forecast of thermal-hydrological conditions and air injection test results of the Single Heater Test at Yucca Mountain. Yucca Mountain Site Characterization Project Report LBNL-39789, E.O. Lawrence Berkeley National Laboratory, Berkeley, California.
- Bodvarsson, G.S., T.M. Bandurraga, and Y.-S. Wu, eds., 1997. The site-scale unsaturated zone model of Yucca Mountain, Nevada, for the Viability Assessment, Yucca Mountain Site

Characterization Project Report LBL-40376, UC814, E. O. Lawrence Berkeley National Laboratory, Berkeley, CA.

Brodsky, N. S., M. Riggins, J. Connolly and P. Ricci, 1997. Thermal conductivity and heat capacity measurements for boreholes UE25 NRG-4, UE25 NRG-5, USW NRG-6, and USW NRG-7/7a, SAND 95-1955, Sandia National Laboratories, Albuquerque, NM.

Buscheck, T.A. , D.G. Wilder and J.J. Nitao, 1993. Repository-heat-driven hydrothermal flow at Yucca Mountain, Part II: Large scale in situ heater tests, *Nuclear Technology*, Vol. 104, No.3, pp. 449-471.

Buscheck, T.A. and J.J. Nitao, 1993. Repository-heat-driven hydrothermal flow at Yucca Mountain, Part I: Modeling and Analysis, *Nuclear Technology*, Vol. 104, No.3, pp. 418-448.

Buscheck, T.A., and J. J. Nitao, 1992. The impact of thermal loading on repository performance at Yucca Mountain: Report UCRL-JC-109232, Lawrence Livermore National Laboratory, Livermore, CA.

CRWMS M&O, 1996. Characterization of the ESF Thermal Test Area, Report B00000000-01717-5705-00047, TRW Environmental safety Systems Inc., Las Vegas, Nevada.

CRWMS M&O, 1997. Single Heater Test Status Report, report BAB000000-01717-5700-00002, TRW Environmental Safety Systems Inc., Las Vegas, Nevada.

Edlefsen, N.E. and A.B.C. Anderson, 1943. Thermodynamics of soil moisture, *Hilgardia*, Vol. 15, no. 2, pp. 31-298.

Flint, A.L., J.A. Hevesi, and L.E. Flint, (in preparation). Conceptual and numerical model of infiltration for the Yucca Mountain area, Nevada, U.S. Geological Survey Water-Resources Investigation Report, U.S. Geological Survey, Denver, CO.

Flint, L.E., (in preparation). Matrix properties of hydrogeologic units at Yucca Mountain, Nevada, U.S. Geological Survey Open-File Report, U.S. Geological Survey, Denver, CO.

Freifeld, B., and Y. Tsang, 1997. Letter report on first quarter results of measurements in hydrology holes in single heater test area in the ESF. Yucca Mountain Site Characterization Project Report, Lawrence Berkeley National Laboratory, Berkeley, CA.

Glassley, W. 1997. Third quarter report, chemical analyses of waters collected from the Single Heater Test area. Yucca Mountain Site Characterization Project Report, Lawrence Livermore National Laboratory, Livermore, CA.

Guzman, A.G., A.M. Geddis, M.J. Henrich, C.F. Lohrstorfer, and S.P. Neuman, 1996. Summary of air permeability data from single-hole injection tests in unsaturated fractured tuffs at the Apache Leap Research Site; Results of steady-state interpretation, U.S. Nuclear Regulatory Commission Report NUREG/CR-6360, NRC, Washington DC.

- Hvorslev, M.J., 1951. Time lag and soil permeability in groundwater observations, Bulletin 36, U.S. Army Corps of Engineers, Water Ways Experimental Station, Vicksburg, Michigan.
- LeCain, G.D., 1995. Pneumatic testing in 45-degree-inclined boreholes in ash-flow tuff near Superior, Arizona, USGS Water Resources Investigations Report 95-4073, USGS, Denver, Colorado.
- LeCain, G.D., 1997. Air injection testing in vertical boreholes in welded and nonwelded tuff, Yucca Mountain, Nevada, U.S. geological Survey Water-Resources Investigation Report 96-4262, U.S. geological Survey, Denver, CO.
- Mualem, Y., 1976. A new model for predicting the hydraulic conductivity of unsaturated porous media, *Water Resources Research*, vol. 12, pp. 513-522.
- Peterson, J. E., and K.H. Williams, 1997. To assess the effectiveness of the ground penetrating radar method in measuring moisture content in the Single Heater Test. Yucca Mountain Site Characterization Project Report, Lawrence Berkeley National Laboratory, Berkeley, CA.
- Pruess, K. and Y. Tsang, 1994. Thermal modeling for a potential High-Level Nuclear Waste Repository at Yucca Mountain, Nevada. Report LBL-35381, Lawrence Berkeley National Laboratory, Berkeley, CA.
- Pruess, K., 1987. TOUGH user's guide, Lawrence Berkeley National Laboratory report LBL-20700, Berkeley, CA.
- Pruess, K., 1991. TOUGH2 — A general purpose numerical simulator for multiphase fluid and heat flow, Technical Report LBL-29400, UC-251, Lawrence Berkeley National Laboratory, Berkeley, CA.
- Pruess, K., J. S. Y. Wang and Y. W. Tsang, 1990. On thermohydrologic conditions near high-level nuclear wastes emplaced in partially saturated fractured tuff 2. Effective continuum Approximation, *Water Resources Research*, 26(6), 1249-1261.
- Rousseau, J.P., E.W. Kwicklis, and D.C. Gilles, eds., (in preparation). Hydrogeology of the unsaturated zone, North Ramp area of exploratory studies facility, Yucca Mountain, Nevada, U.S. Geological Survey Water-Resources Investigations Report, U. S. Geological Survey, Denver, Colorado.
- SNL 1996. Thermal Properties of Test Specimens from the Single Heater Test Area in the Thermal Testing Facility at Yucca Mountain, Nevada.. Yucca Mountain Site Characterization Project Report. Sandia National Laboratories, Albuquerque, New Mexico.
- SNL 1997. Evaluation and comparative analysis of Single Heater Test thermal and thermomechanical data: Third Quarter Results (8/26/96 through 5/31/97). Yucca Mountain Site Characterization Project Report. Sandia National Laboratories, Albuquerque, New Mexico.
- Sobolik, S.R., N.D. Francis, J. Pott, Pre-experiment thermal-hydrological-mechanical analyses for the ESF Single Heater Test, Sandia National Laboratories Letter Report SLTR96-0004, 1996.

- Sonnenthal, E., R. Ahlers, and G.S. Bodvarsson, 1997. Fracture and fault properties for the UZ site-scale flow model, Chapter 7 of The site-scale unsaturated zone model of Yucca Mountain, Nevada, for the Viability Assessment, G.S. Bodvarsson, T.M. Bandurraga, and Y.-S. Wu, eds., Yucca Mountain Site Characterization Project Report, Lawrence Berkeley National Laboratory Report, Berkeley, CA.
- Tsang, Y.W., and K. Pruess, 1987. A study of thermally induced convection near a high-level nuclear waste repository in partially saturated fractured tuff, *Water Resources Research*, 23(10), 1958-1966.
- Tsang, Y.W., J. Wang, B. Freifeld, P. Cook, R. Suarez-Rivera, and T. Tokunaga, 1996. Letter report on hydrological characterization of the single heater test area in the ESF. Yucca Mountain Site Characterization Project Report, Lawrence Berkeley National Laboratory, Berkeley, CA.
- Van Genuchten, M.T., 1980. A closed-form equation for predicting the hydraulic conductivity of unsaturated soil, *Soil Sci. Soc. Am. J.*, vol. 44, no. 5, pp. 892-898.
- Vargaftik, N.B., 1975. Tables of the Thermophysical Properties of Liquids and Gases in Normal and Dissociated States, John Wiley & Sons, Inc., ACCN: NNA.19940428.0016, 2nd Edition.
- Walker, W.R., J.D. Sabey, and D.R. Hampton, 1981. Studies of heat transfer and water migration in soils, Final Report, Department of Agricultural and Chemical Engineering, Colorado University, Fort Collins, CO.
- Wang, J. and R. Suárez-Rivera, 1997. Laboratory test results of hydrological properties from dry drilled and wet drilled cores in the drift scale test area and in the single heater test area of the thermal test facility. Yucca Mountain Site Characterization Project Report, Lawrence Berkeley National Laboratory, Berkeley, CA.

Nomenclature

D_{va}	Diffusion coefficient for the vapor-air mixture in a porous medium (m^2/s)
D_{va}^o	Free-space diffusion coefficient
k	Permeability (m^2)
k_m	Matrix continuum permeability (m^2)
k_f	Fracture continuum permeability (m^2)
$k_{r,l}$	Liquid relative permeability
$k_{r,g}$	Gas relative permeability
$k_{r,m}$	Matrix relative permeability
$k_{r,f}$	Fracture relative permeability
k_b	Effective continuum permeability of fluid phase b (m^2)
L	Length of air injection zones (m)
m_l	molecular weight of liquid
$m = 1 - 1/\beta$	van Genuchten parameter for characteristic curves
P_1, P_2	Initial pressure and final steady state pressure for air injection tests (Pa)
P_{sc}	Pressure at standard conditions, 1.013×10^5 Pa
P_{cap}	Capillary pressure (Pa)
P_v	Vapor pressure (Pa)
P_{sat}	Saturated vapor pressure (Pa)
R	Universal gas constant
Q_{sc}	Flowrate at standard conditions in air injection tests (m^3/s)
r_w	Radius of boreholes (m)
$S_{b,m}$	Effective continuum phase saturation in matrix
$S_{b,f}$	Effective continuum phase saturation in fracture
$S_{l,eff}$	Liquid effective saturation
S_g	Gas saturation
T	Temperature ($^{\circ}C$)
T_f	Temperature of formation in air injection tests ($^{\circ}K$)
T_{SC}	Temperature at standard conditions ($273.15^{\circ}K$)
α	van Genuchten parameter for characteristic curves, $(Pa)^{-1}$, $1/\alpha$ is the air entry pressure
β	van Genuchten parameter, pore size distribution coefficient
ϕ	porosity
ϕ_m	Matrix porosity
ϕ_f	Fracture porosity
λ	Brooks-Corey relative permeability curve parameter
μ	Dynamic viscosity of air (Pa-s), 1.81×10^{-5} at $20^{\circ}C$
θ	Temperature dependence factor for vapor diffusion
ρ_l	Liquid density (kg/m^3)
τ	Tortuosity

Appendix

Some key equations for the processes included in the numerical simulations are as follows. Matrix and fracture continua are given the same functional dependence in the characteristic curves. The capillary suction and the relative permeability for liquid have the van Genuchten functional forms:

$$\begin{aligned}
 P_{cap} &= -\frac{1}{\alpha} \left\{ (S_{l,eff})^{-\frac{1}{m}} - 1 \right\}^{\frac{1}{\beta}} \\
 k_{r,l} &= (S_{l,eff})^{\frac{1}{2}} \left\{ 1 - \left(1 - (S_{l,eff})^{\frac{1}{m}} \right)^m \right\}^2 \\
 \beta &= \frac{1}{(1-m)} \\
 S_{l,eff} &= \frac{(S_l - S_r)}{(S_s - S_r)}
 \end{aligned} \tag{A1}$$

For the relative permeability to gas we do not apply the common formulation as $(1 - k_{r,l})$ because the van Genuchten functional dependence has an extremely steep slope for liquid relative permeability near full liquid saturation, giving rise to unrealistically large gas relative permeability values even for very small gas saturation. Therefore, we choose the Brooks-Corey formulation

$$k_{r,g} = (1 - S_{l,eff})^2 \left(1 - S_{l,eff}^{\left(\frac{2+\lambda}{\lambda} \right)} \right) \tag{A2}$$

In the effective-continuum approximation, the fracture and matrix continua are characterized by the same temperature and pressure, where the effective continuum saturation S_b is given by:

$$S_b = \frac{S_{b,m}\phi_m + S_{b,f}\phi_f}{\phi_m + \phi_f} \tag{A3}$$

and the effective-continuum phase permeability k_b is :

$$k_b = k_m k_{r,m} + k_f k_{r,f} \tag{A4}$$

The diffusion coefficient D_{va}^o for the vapor-air mixture in a porous medium is given by Vargaftik, 1975; and Walker et al., 1981

$$D_{va} = \tau \phi S_g D_{va}^o \frac{P_{SC}}{P} \left[\frac{T}{T_{SC}} \right]^\theta \quad (A5)$$

The vapor pressure lowering effect is represented by Kelvin's equation (Edlefsen and Anderson, 1943)

$$f_{VPL} = \frac{P_v(T, S_l)}{P_{sat}(T)} = \exp \left(\frac{m_l P_{cap}(S_l)}{\rho_l R (T + 273.15)} \right) \quad (A6)$$

where f_{VPL} , the vapor pressure lowering factor is identical to the definition of relative humidity. The readings in the relative humidity sensor can serve to monitor the evolution of the dry-out region where the capillary pressure P_{cap} attains a very strong negative value.

The saturation dependence of the thermal conductivity is given by:

$$C(S_l) = C_{dry} + (C_{wet} - C_{dry}) \sqrt{S_l} \quad (A7)$$

Table 1. Hydrological and thermal input values

Parameter	Value	Comments
Matrix Porosity	0.11	Flint, 1996
Matrix Permeability	$4.0 \times 10^{-18} \text{ m}^2$	Flint, 1996
Matrix van Genuchten parameter α	$6.4 \times 10^{-7} \text{ Pa}^{-1}$	Flint, 1996
Matrix van Genuchten parameter $\beta = 1/(1-m)$	1.47	Flint, 1996
Brooks Corey parameter λ for gas phase permeability	2	
Matrix Residual Liquid Saturation	0.18	
Matrix Grain Density	2540.0 kg/m^3	SHT laboratory measurements
Initial Matrix Liquid Saturation	0.92	SHT laboratory measurements
Fracture Porosity	0.000243	Bodvarsson et al., 1996.
Fracture Permeability (low permeability background)	$5.85 \times 10^{-14} \text{ m}^2$	SHT field measurements
Fracture Permeability (high-permeability feature)	$5.2 \times 10^{-12} \text{ m}^2$	SHT field measurements
Fracture van Genuchten α	$1.0 \times 10^{-3} \text{ Pa}^{-1}$	Bodvarsson et al., 1997.
Fracture van Genuchten β	1.47	Bodvarsson et al., 1997.
Fracture Residual Liquid Saturation	0.01	Bodvarsson et

Parameter	Value	Comments
		al., 1997.
Rock Mass Thermal Conductivity $C(S_l) = C_{dry} + (C_{wet} - C_{dry})\sqrt{S_l}$	$C_{dry} = 1.67 \text{ W/(m } ^\circ\text{K)}$ $C_{wet} = 2.0 \text{ W/(m } ^\circ\text{K)}$	SNL 1996; Brodsky et al., 1997 SHT laboratory measurements
Rock Mass Heat Capacity	953.0 J/(kg $^\circ\text{K}$)	Brodsky et al., 1997. ESF thermal test laboratory measurements
Heater Power (9-month average data)	3758 W	SHT heating phase data
Vapor Diffusion Coefficient D_{va}^0 Temperature dependence θ	$2.14 \times 10^{-5} \text{ m}^2/\text{s}$ 2.334	Pruess and Tsang, 1994

Figure Captions

- Figure 1a. Schematic of borehole layout in the SHT (3D perspective).
- Figure 1b. Borehole layout in the SHT (plan view and cross section).
- Figure 2. A schematic diagram of the coupled thermal-hydrological processes in the SHT.
- Figure 3. Local air permeability estimated from pre-heat air injection tests in 21 boreholes in the SHT block.
- Figure 4. Flow and interference pressure responses of a typical air injection test performed in the pre-heat characterization of fracture permeability.
- Figure 5. Numerical grids for simulation of the SHT.
- Figure 6. Temperature data from boreholes 2, 3, 4, 5, 8, 9, 10, 11, 12, 13, 14, 15, 16, 17, 18, 22, 23.
- Figure 7. Measured and simulated temperature at 3 months, for the dual permeability conceptual model, for temperature sensors in the center-plane of the SHT block at $y = 4.5$ m.
- Figure 8. Measured and simulated temperature at 9 months, for the dual permeability conceptual model, for temperature sensors in the center-plane of the SHT block at $y = 4.5$ m.
- Figure 9. Measured and simulated temperature history, with the dual permeability conceptual model, for all boreholes parallel to Heater Hole 1, for temperature sensors in the center-plane of the SHT block.
- Figure 10. Measured and simulated temperature at 9 months for heat-conduction-only model, for temperature sensors in center-plane of the SHT block. Heat conductivity is $1.67 \text{ W/(m}^\circ\text{K)}$.
- Figure 11. Measured and simulated temperature at 9 months for heat-conduction-only mode, for temperature sensors in center-plane of the SHT block. Heat conductivity is $2.0 \text{ W/(m}^\circ\text{K)}$.
- Figure 12. Fracture saturation and liquid flux at 3 months with the dual permeability conceptual model, shown for the center-plane of the SHT block. The xy-diagram shows distribution of saturation and flux along the z-axis at $x=0.0$ m. Positive flux values denote upward flow, negative flux values denote downward flow.
- Figure 13. Matrix saturation and liquid flux at 3 months with the dual permeability conceptual model, shown for the center-plane of the SHT block. The xy-diagram shows distribution of saturation and flux along the z-axis at $x=0.0$ m. Positive flux values denote upward flow, negative flux values denote downward flow.

Figure 14. Fracture saturation and liquid flux at 3 months for simulation with the effective continuum model, shown for the center-plane of the SHT block. The xy-diagram shows distribution of saturation and flux along the z-axis at $x=0.0$ m. Positive flux values denote upward flow, negative flux values denote downward flow.

Figure 15. Matrix saturation and liquid flux at 3 months for simulation with the effective continuum model, shown for the center-plane of the SHT block. The xy-diagram shows distribution of saturation and flux along the z-axis at $x=0.0$ m. Positive flux values denote upward flow, negative flux values denote downward flow.

Figure 16. Measured and simulated temperature at 3 months, for the effective continuum conceptual model, for temperature sensors in the center-plane of the SHT block at $y = 4.5$ m.

Figure 17. Measured and simulated temperature at 9 months, for the effective continuum conceptual model, for temperature sensors in the center-plane of the SHT block at $y = 4.5$ m.

Figure 18. Measured and simulated temperature history, with the effective continuum conceptual model, for all boreholes parallel to Heater Hole 1, for temperature sensors in the center-plane of the SHT block.

Figure 19. Sensitivity of temperature to matrix permeability, at a radial distance of 0.67 from the heater. Simulation is for the dual permeability conceptual model in a x-z vertical plane at $y = 4.5$ m.

Figure 20. Sensitivity of temperature to fracture permeability, at a radial distance of 0.67 m from the heater. Simulation is for the dual permeability conceptual model in a x-z vertical plane at $y = 4.5$ m.

Figure 21. Sensitivity of temperature to matrix a parameter, at a radial distance of 0.67 m from the heater. Simulation is for the dual permeability conceptual model in a x-z vertical plane at $y = 4.5$ m.

Figure 22. Sensitivity of temperature to fracture a parameter, at a radial distance of 0.67 m from the heater. Simulation is for the dual permeability conceptual model in a x-z vertical plane at $y = 4.5$ m.

Single Heater Test

Borehole Perspective

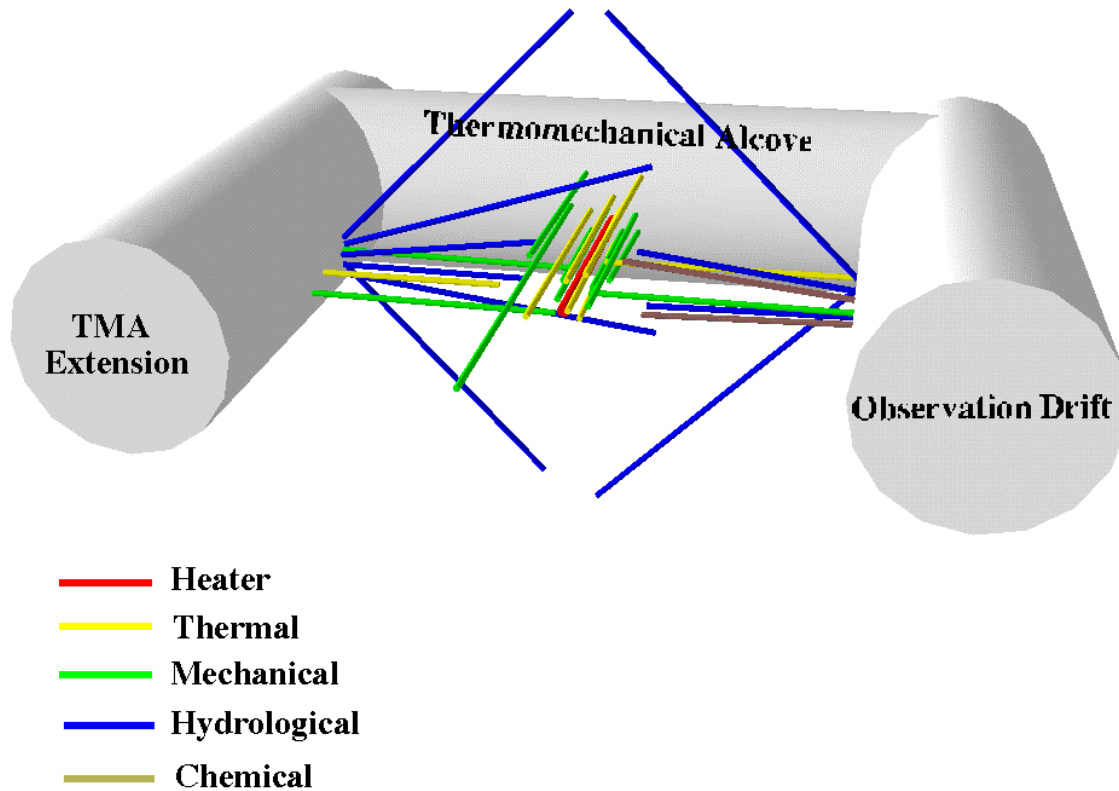


Figure 1a. Schematic of boreholes layout in the SHT (3D perspective)

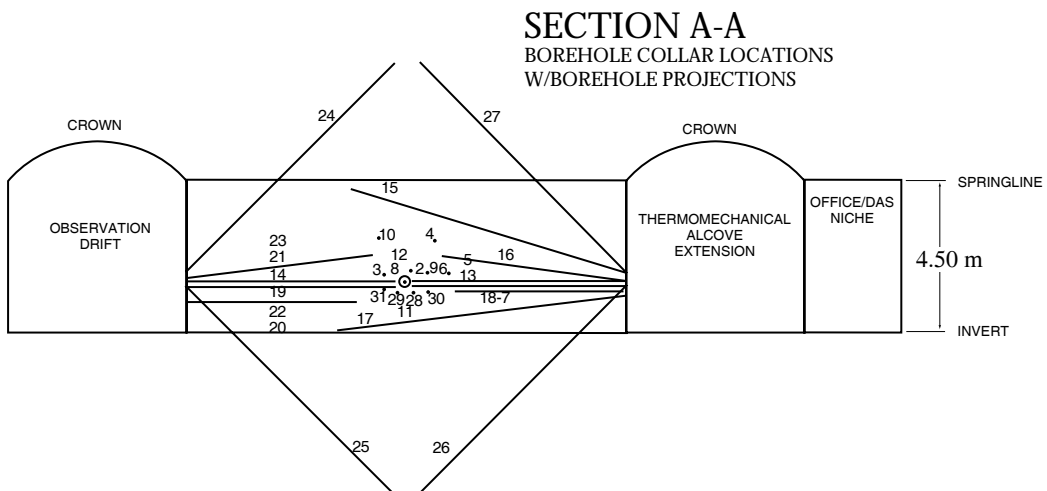
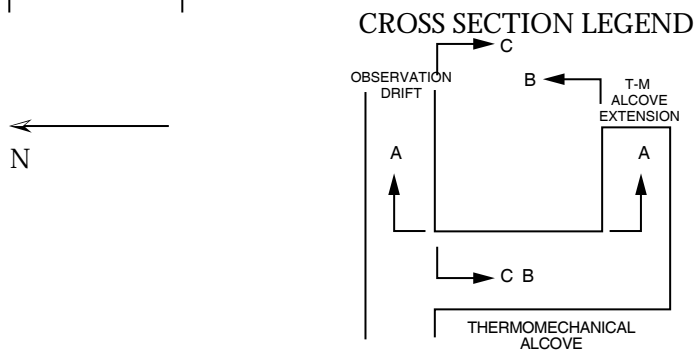
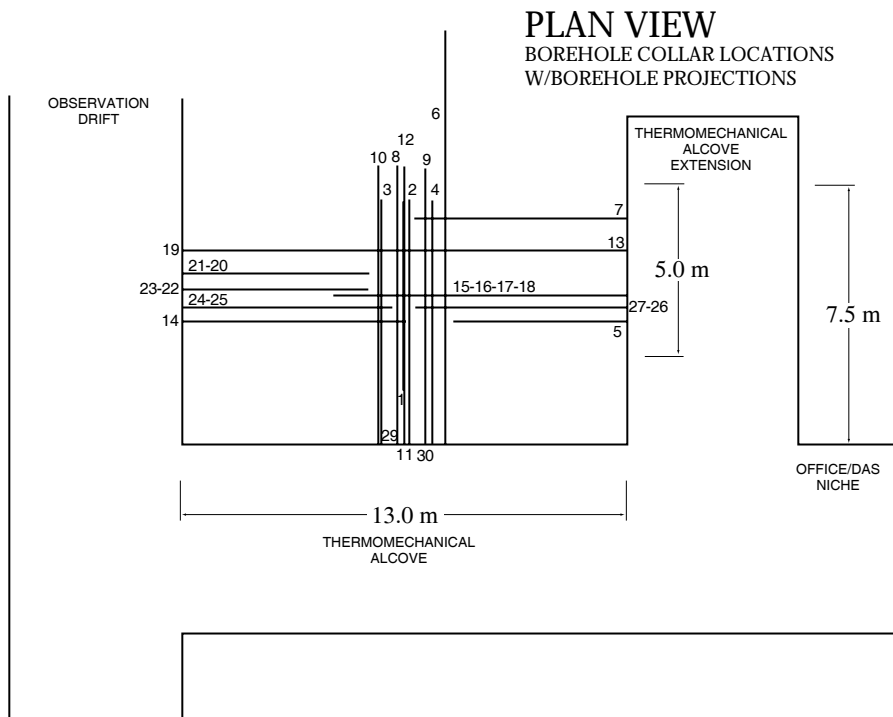


Figure 1b. Borehole layout in the SHT (plan view and cross-section).

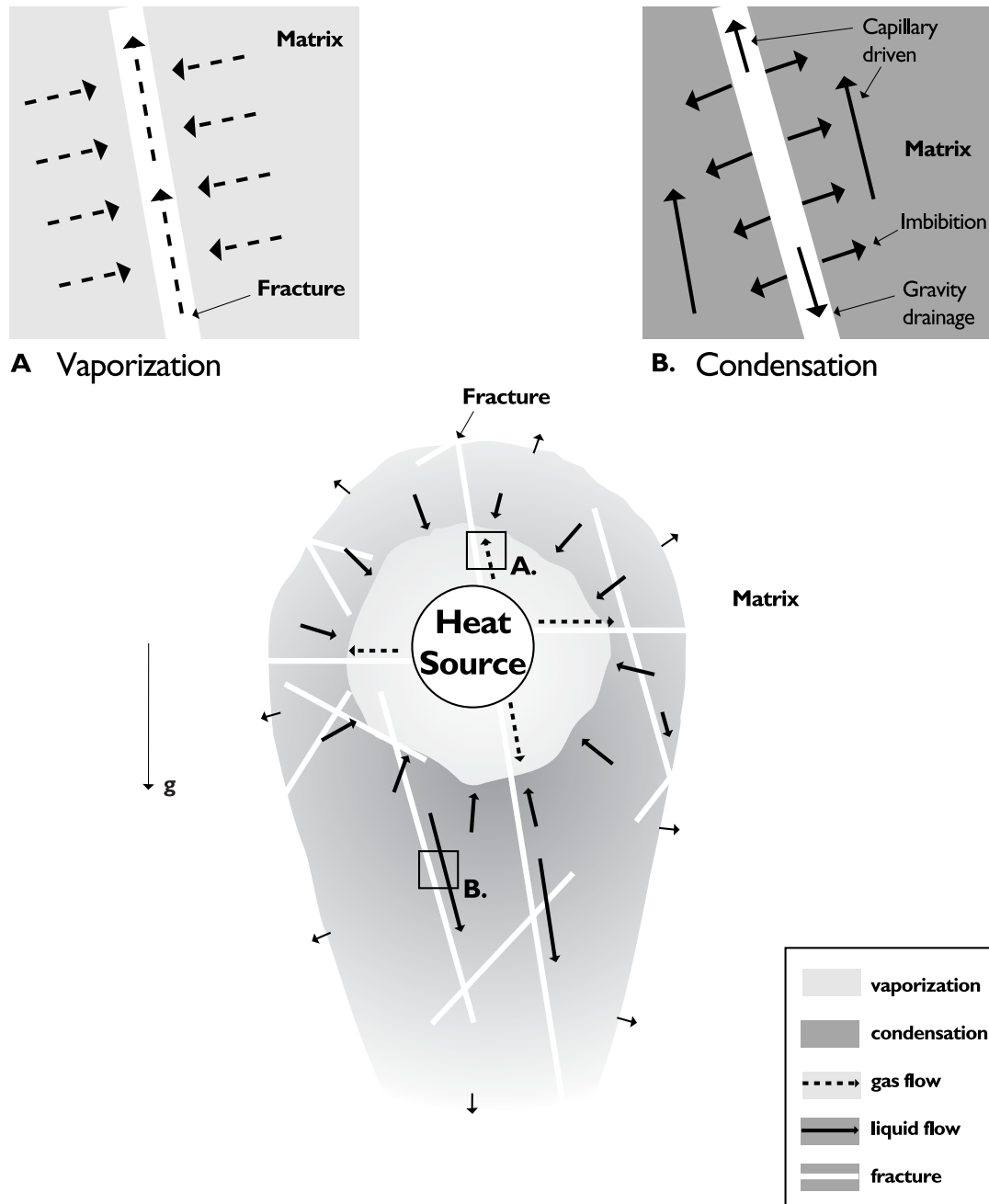


Figure 2. A schematic diagram of the coupled thermal-hydrological process in the SHT.

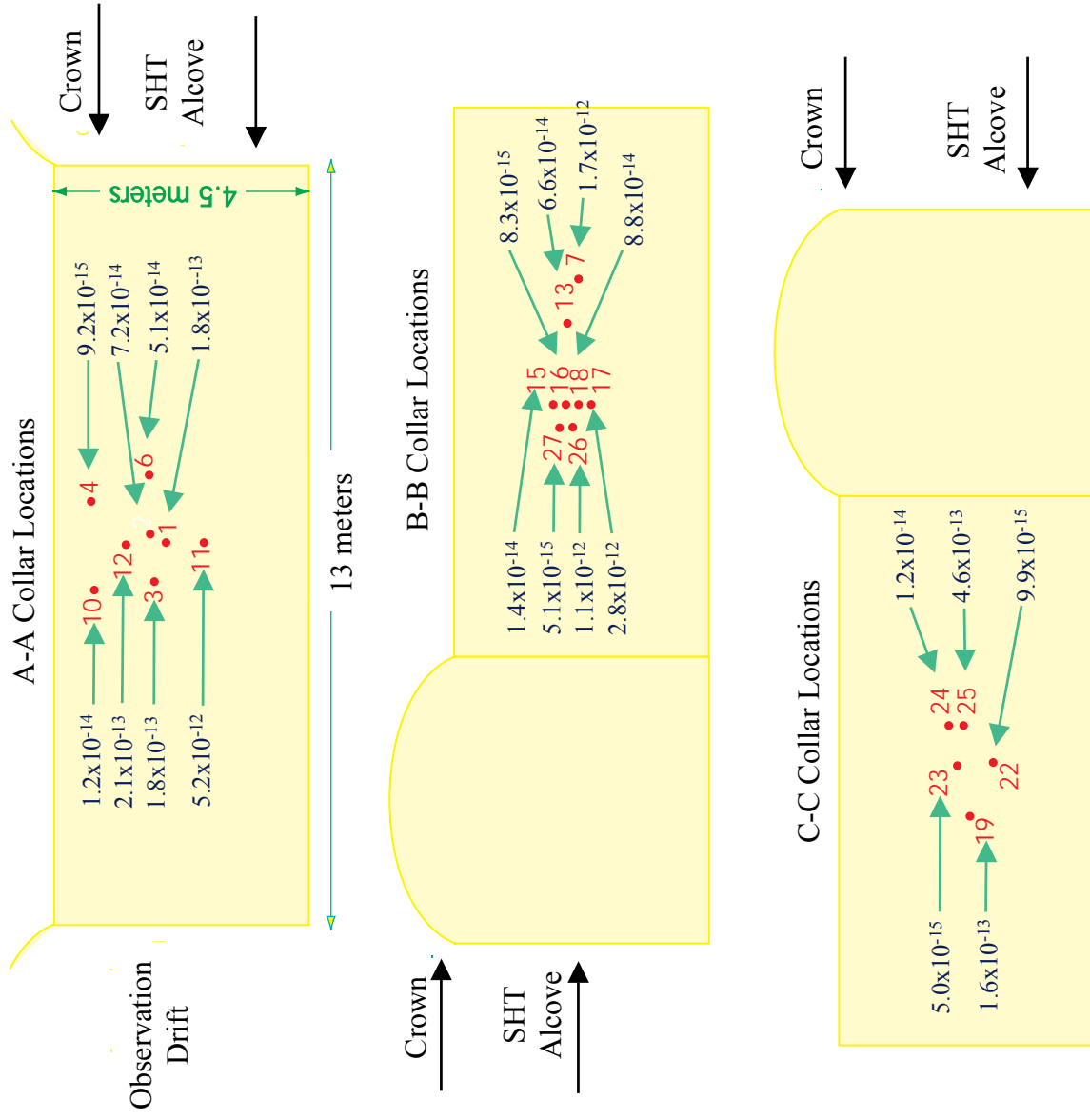


Figure 3. Local air permeability estimated from pre-heating air injection tests in 21 boreholes in the SHT block.

Typical Flow and Interference Pressure Response - 31MAY01

(Injection in Hole #7)

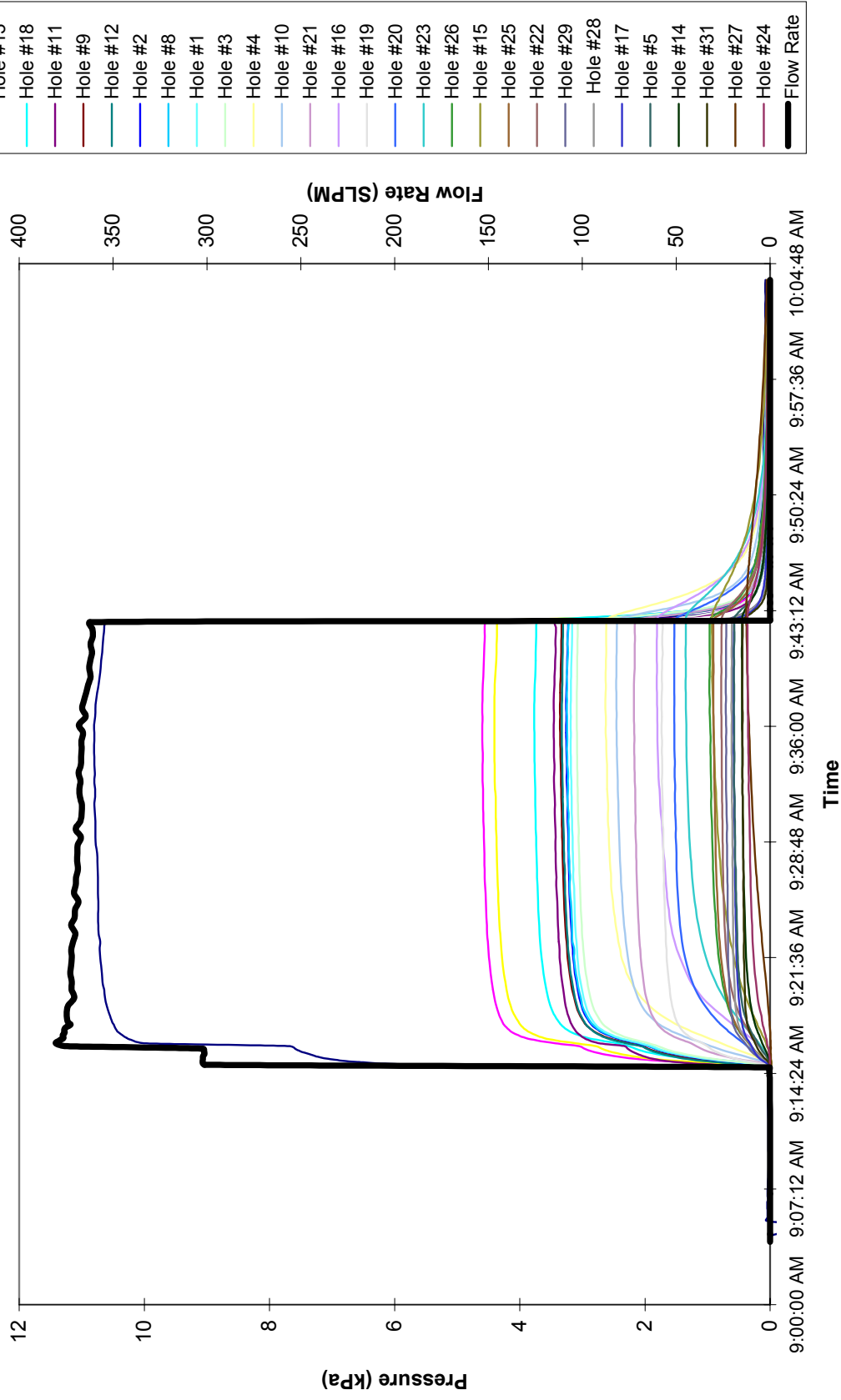


Figure 4. Flow and interference pressure responses of a typical air injection test performed in the pre-heat characterization of fracture permeability.

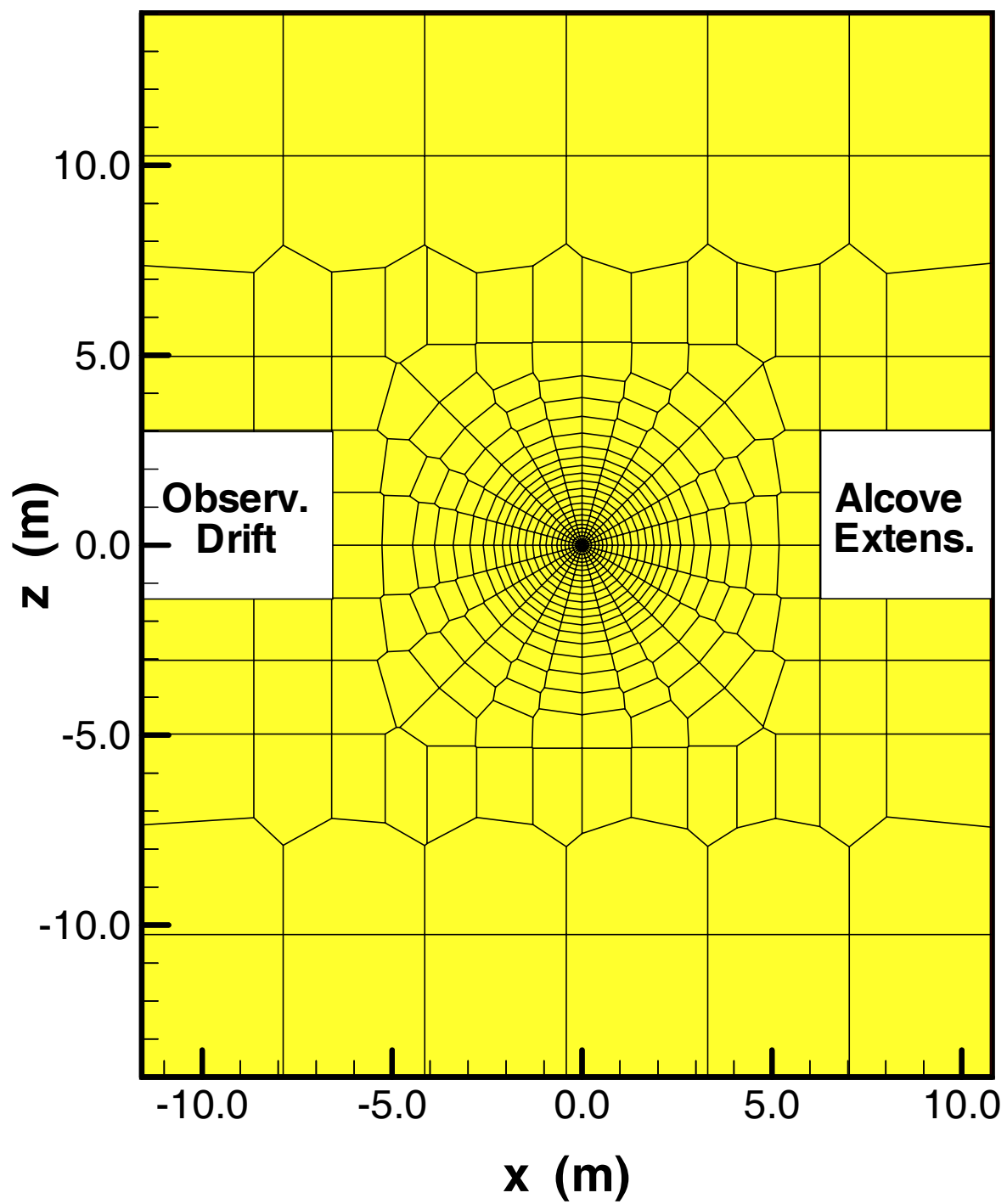


Figure 5a. Numerical grids for simulation of the SHT.

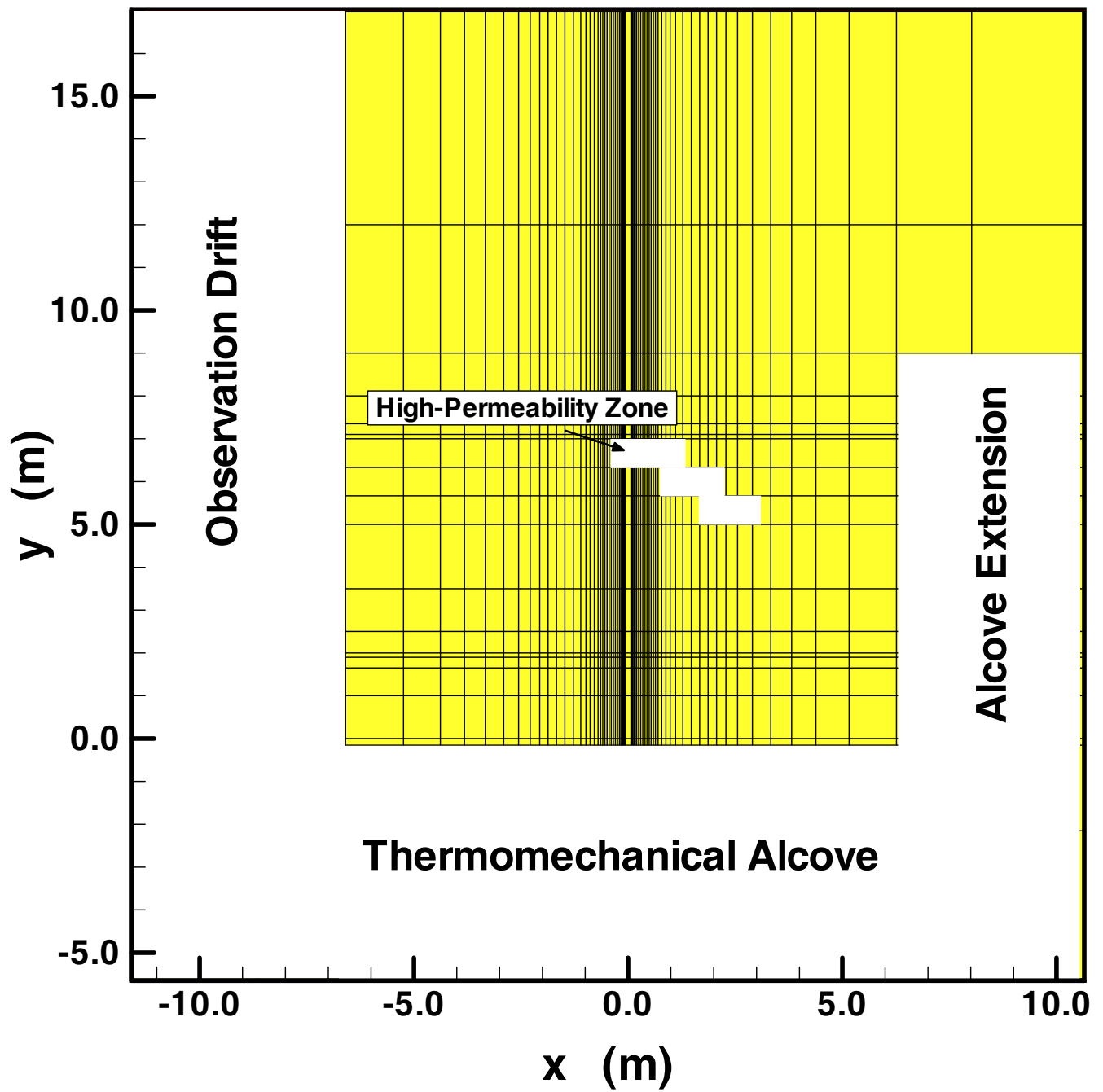


Figure 5b. Numerical grids for simulation of the SHT.

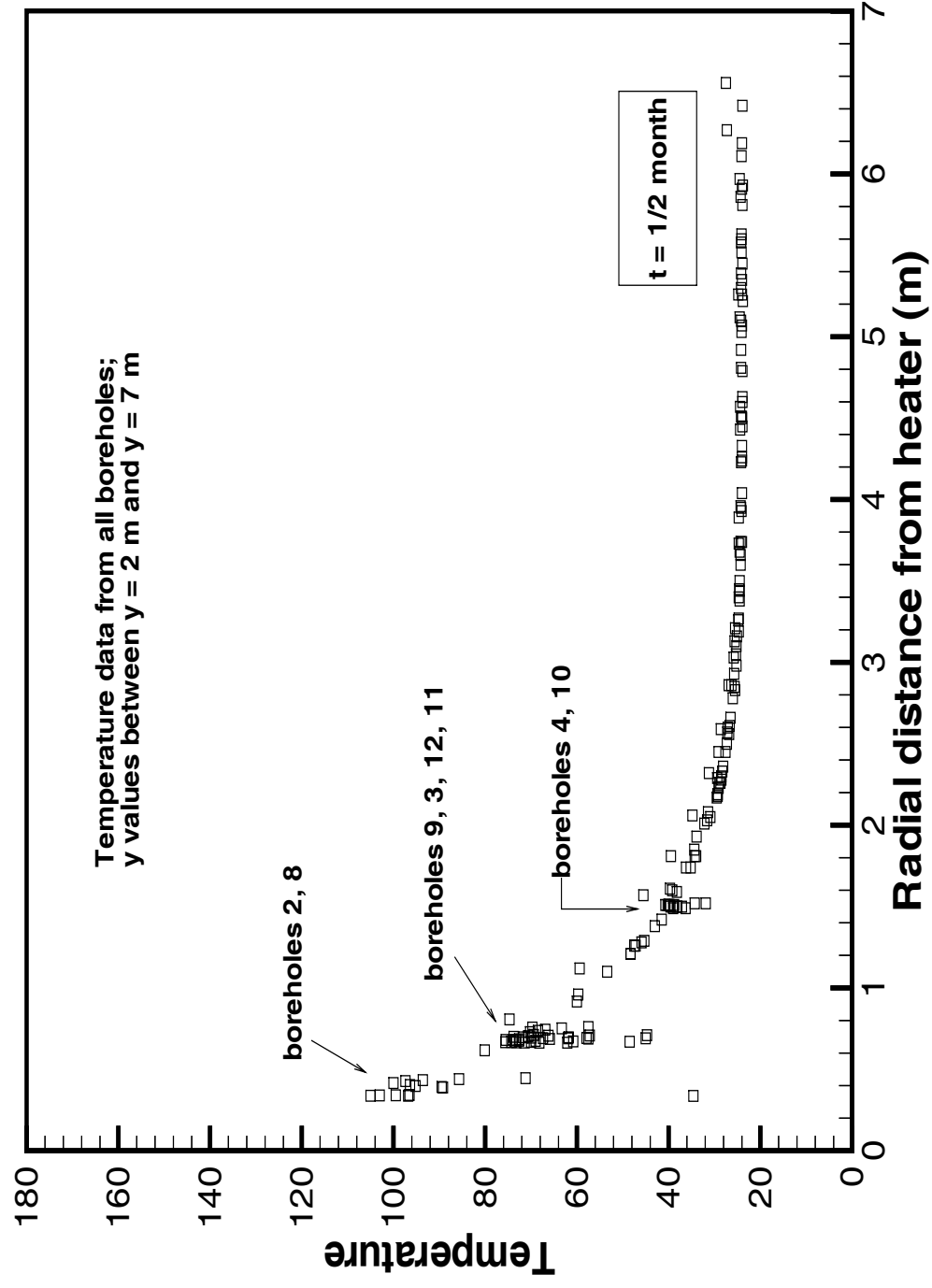


Figure 6. Temperature data from boreholes 2, 3, 4, 5, 8, 9, 10, 11, 12, 13, 14, 15, 16, 17, 18, 22, 23.

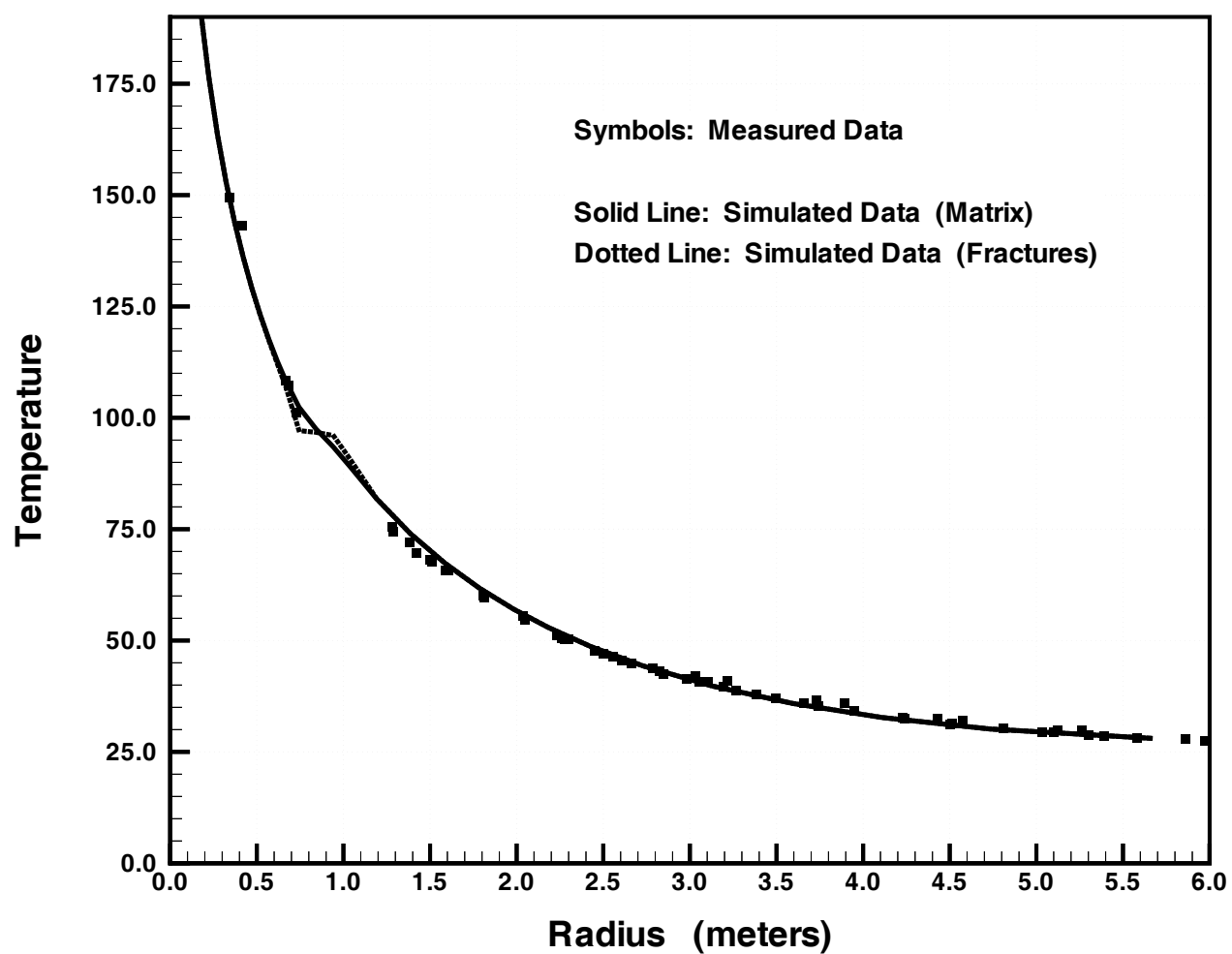


Figure 7. Measured and simulated temperature at 3 months, for the dual permeability conceptual model, for temperature sensors in the center-plane of the SHT block at $y = 4.5$ m.

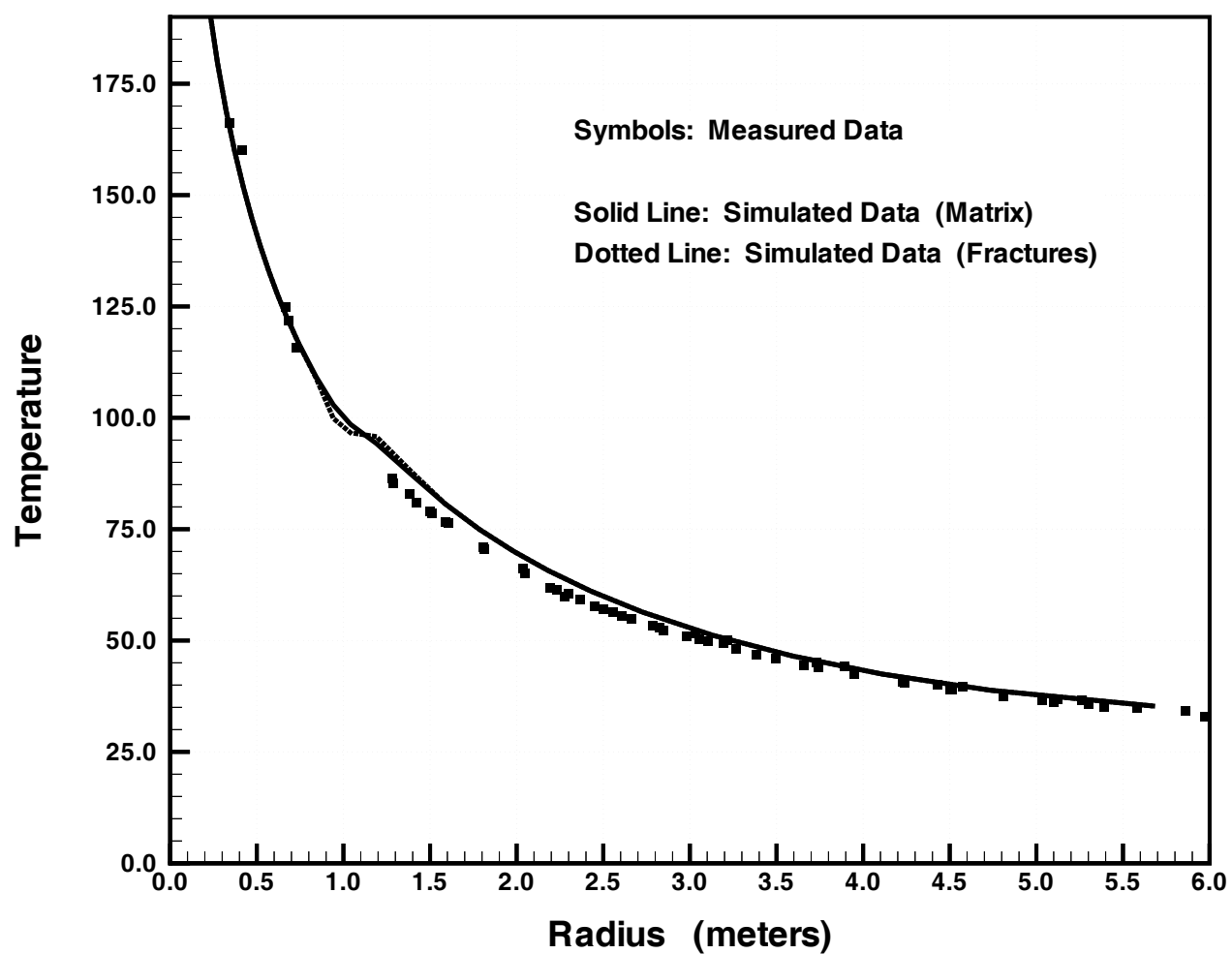


Figure 8. Measured and simulated temperature at 9 months, for the dual permeability conceptual model, for temperature sensors in the center-plane of the SHT block at $y = 4.5$ m.

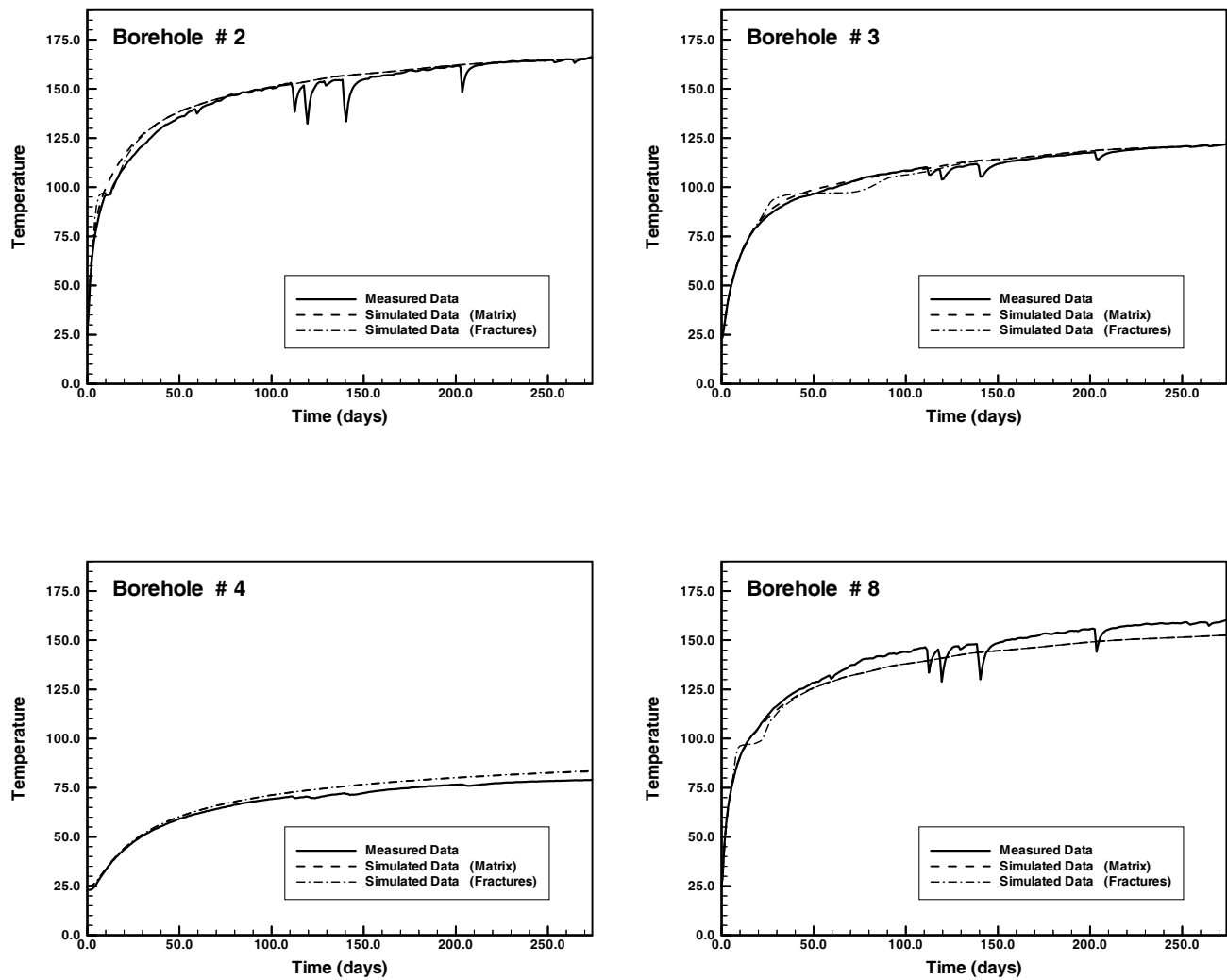
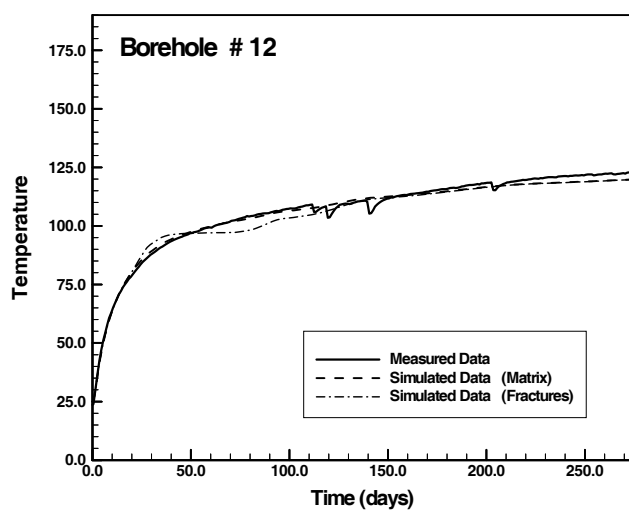
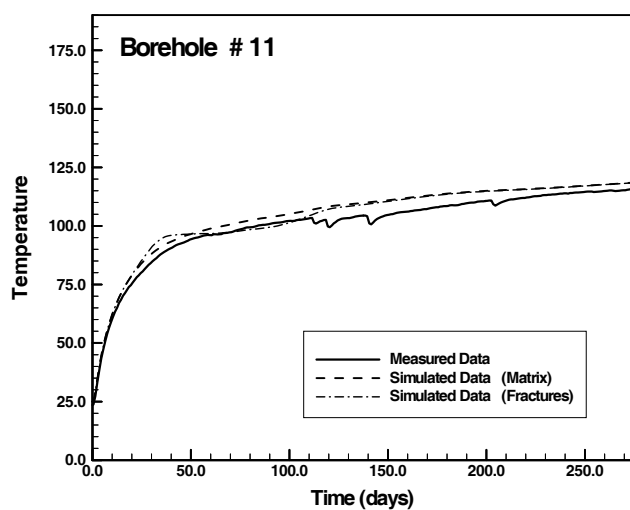
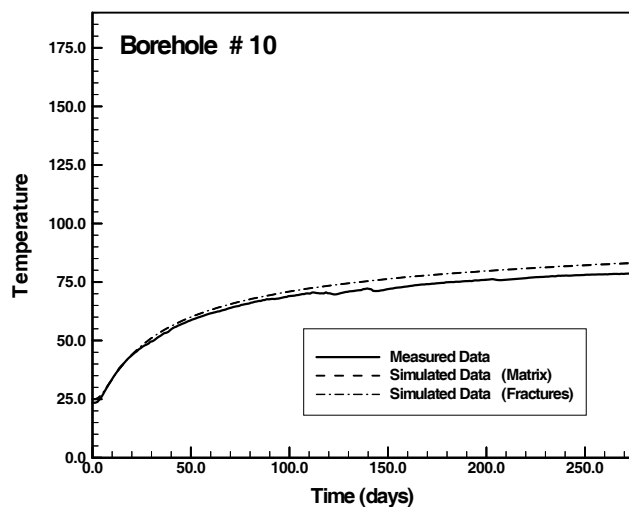
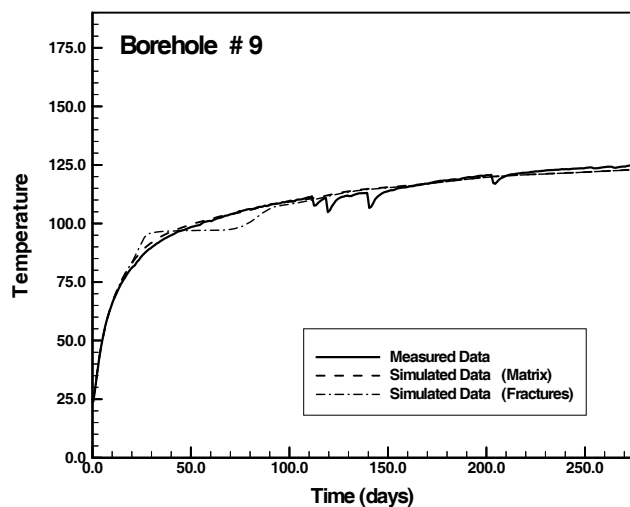


Figure 9. Measured and simulated temperature history, with the dual permeability conceptual model, for all boreholes parallel to Heater Hole 1, for temperature sensors in the center-plane of the SHT block.



cont. Figure 9. Measured and simulated temperature history, with the dual permeability conceptual model, for all boreholes parallel to Heater Hole 1, for temperature sensors in the center-plane of the SHT block.

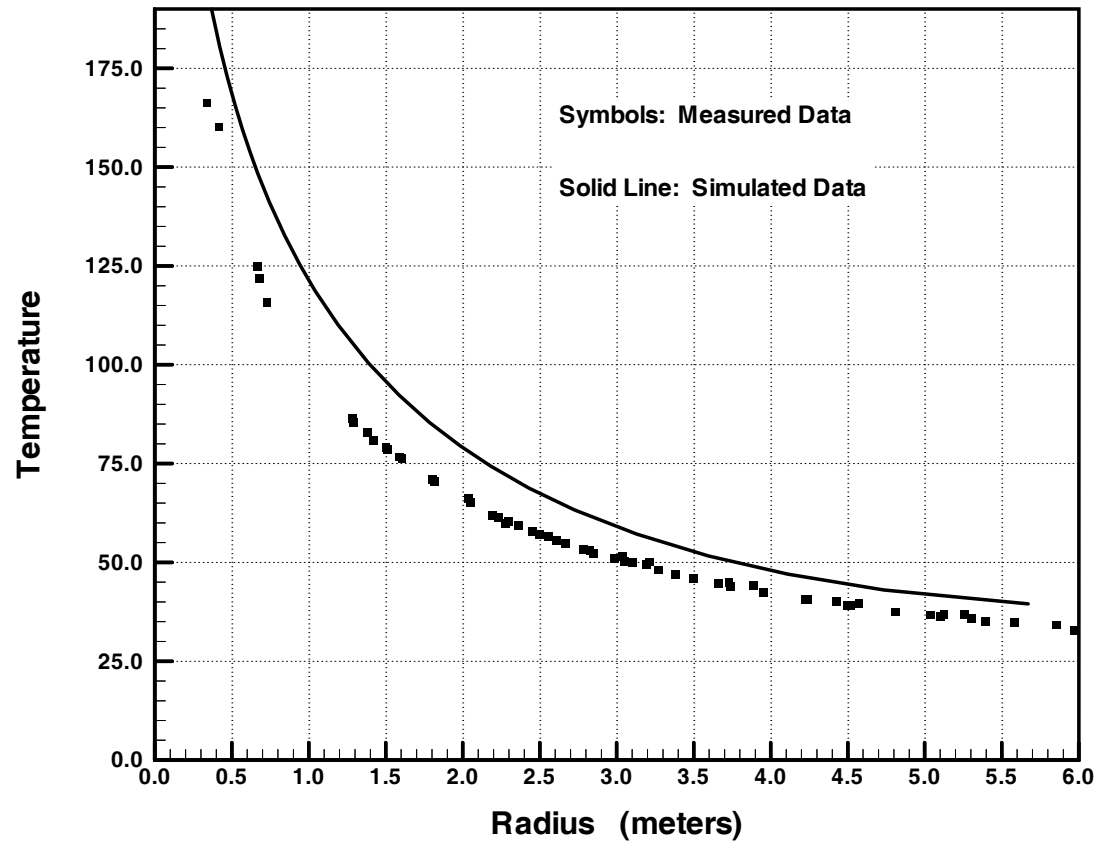


Figure 10. Measured and simulated temperature at 9 months for heat-conduction-only model, for temperature sensors in center-plane of the SHT block. Heat conductivity is $1.67 \text{ W}/(\text{m}^0\text{K})$.

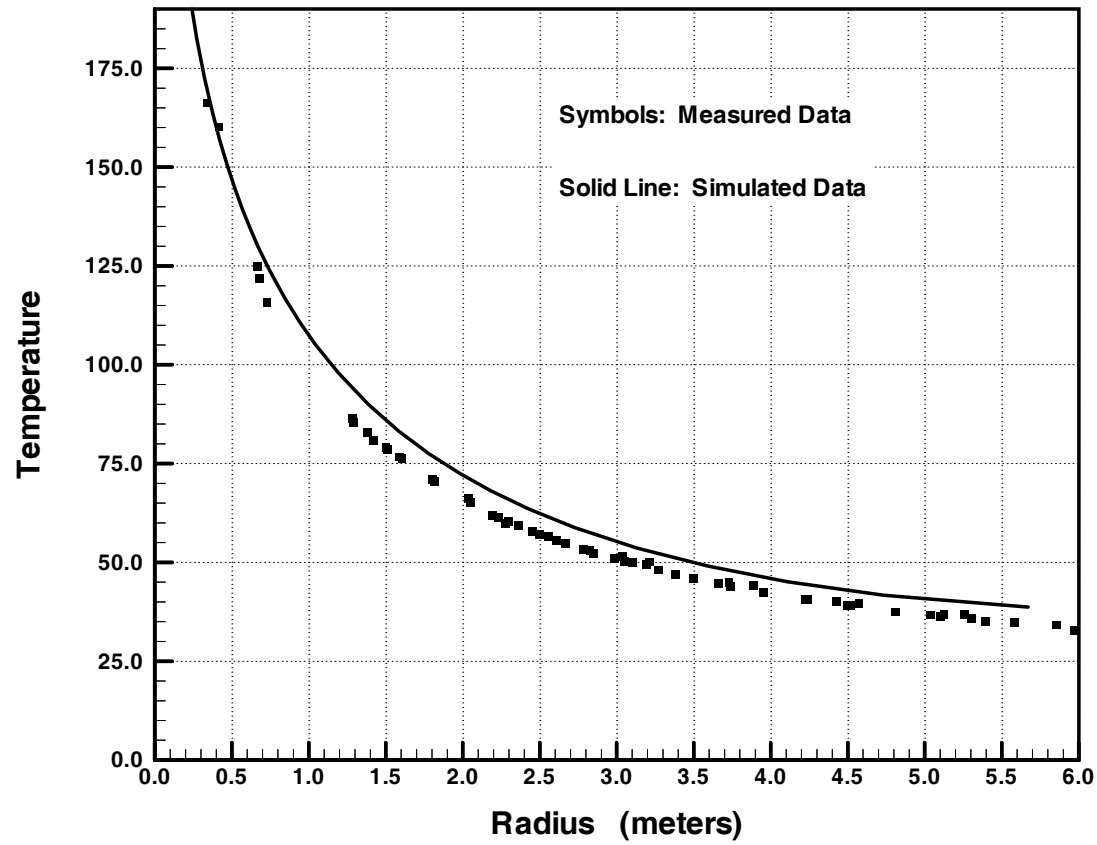


Figure 11. Measured and simulated temperature at 9 months for heat-conduction-only mode, for temperature sensors in center-plane of the SHT block. Heat conductivity is $2.0 \text{ W}/(\text{m}^0\text{K})$.

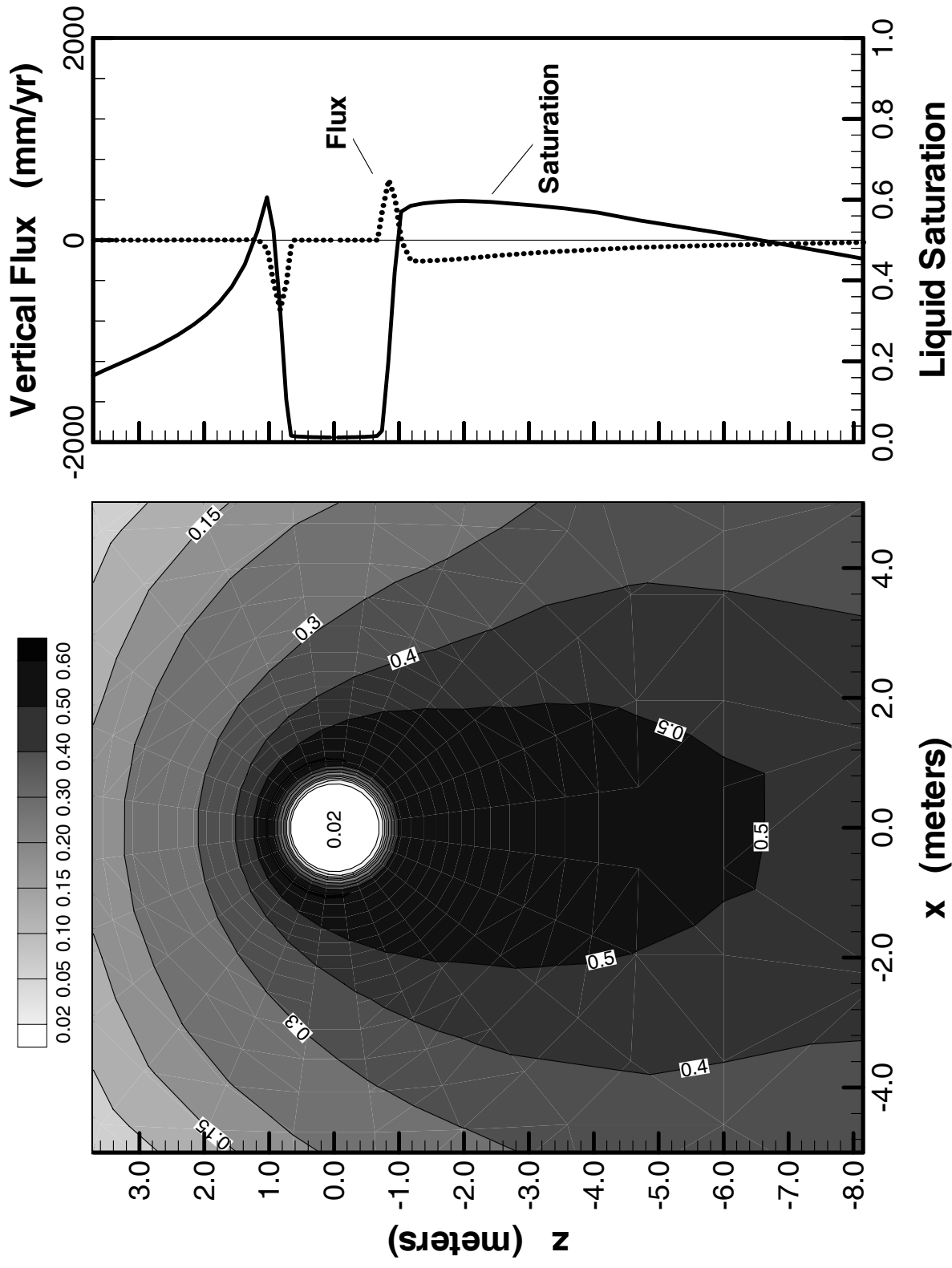


Figure 12. Fracture saturation and liquid flux at 3 months with the dual permeability conceptual model, shown for the center-plane of the SHT block. The xy -diagram shows distribution of saturation and flux along the z -axis at $x=0.0$ m. Positive flux values denote upward flow, negative flux values denote downward flow.

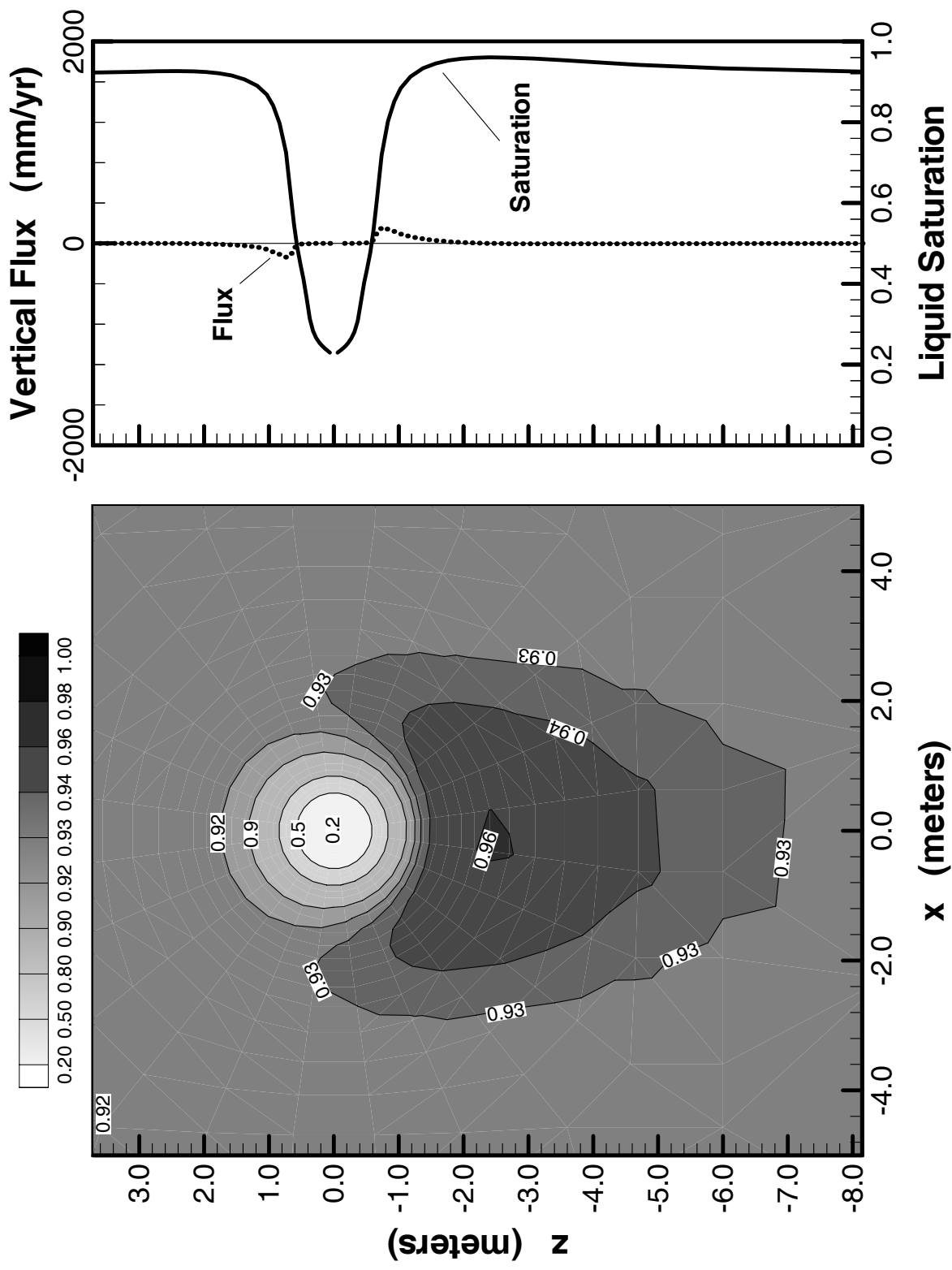


Figure 13. Matrix saturation and liquid flux at 3 months with the dual permeability conceptual model, shown for the center-plane of the SHT block. The xy-diagram shows distribution of saturation and flux along the z-axis at $x=0.0$ m. Positive flux values denote upward flow, negative flux values denote downward flow.

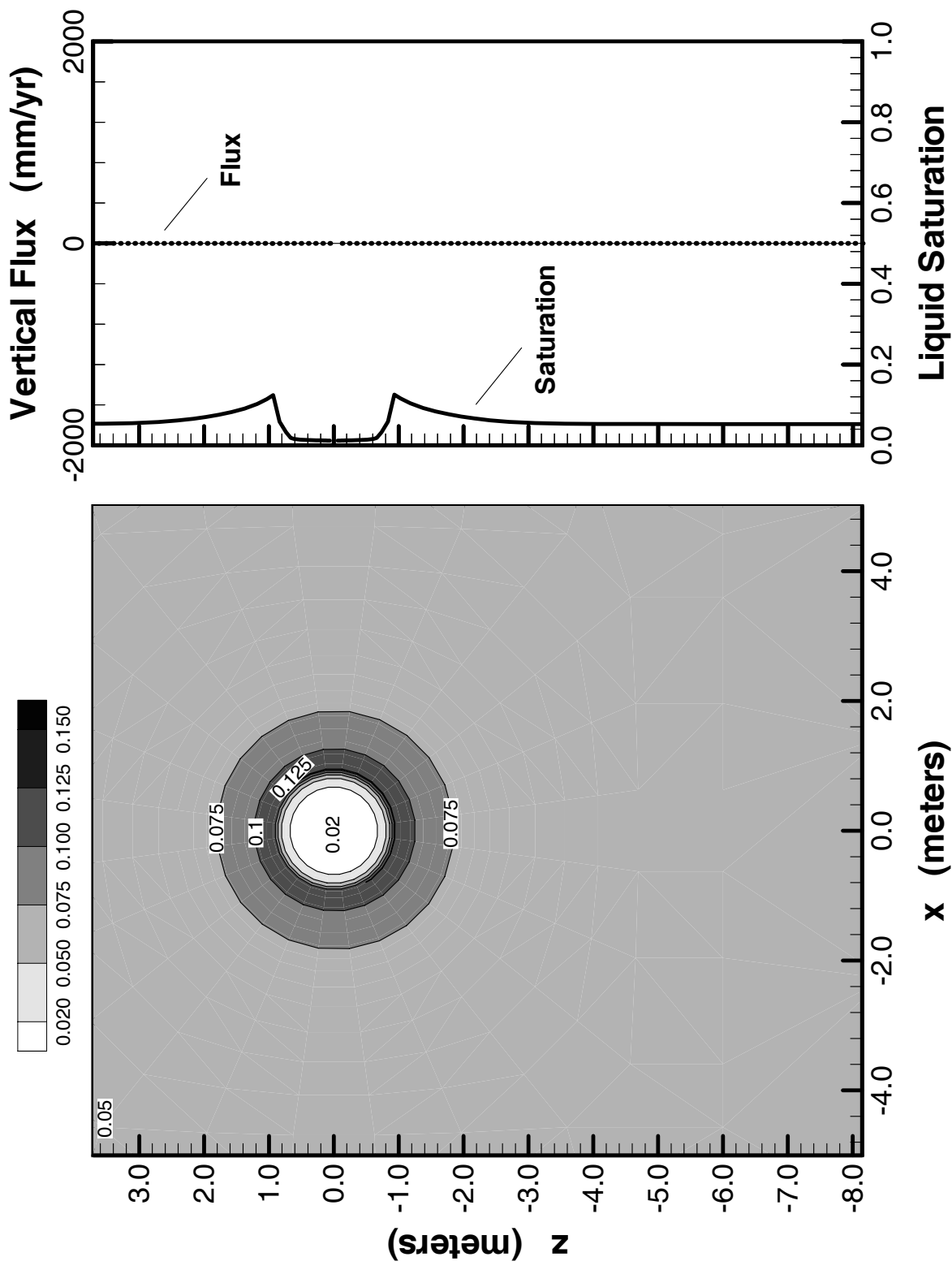


Figure 14. Fracture saturation and liquid flux at 3 months for simulation with the effective continuum model, shown for the center-plane of the SHT block. The xy-diagram shows distribution of saturation and flux along the z -axis at $x=0.0$ m. Positive flux values denote upward flow, negative flux values denote downward flow.

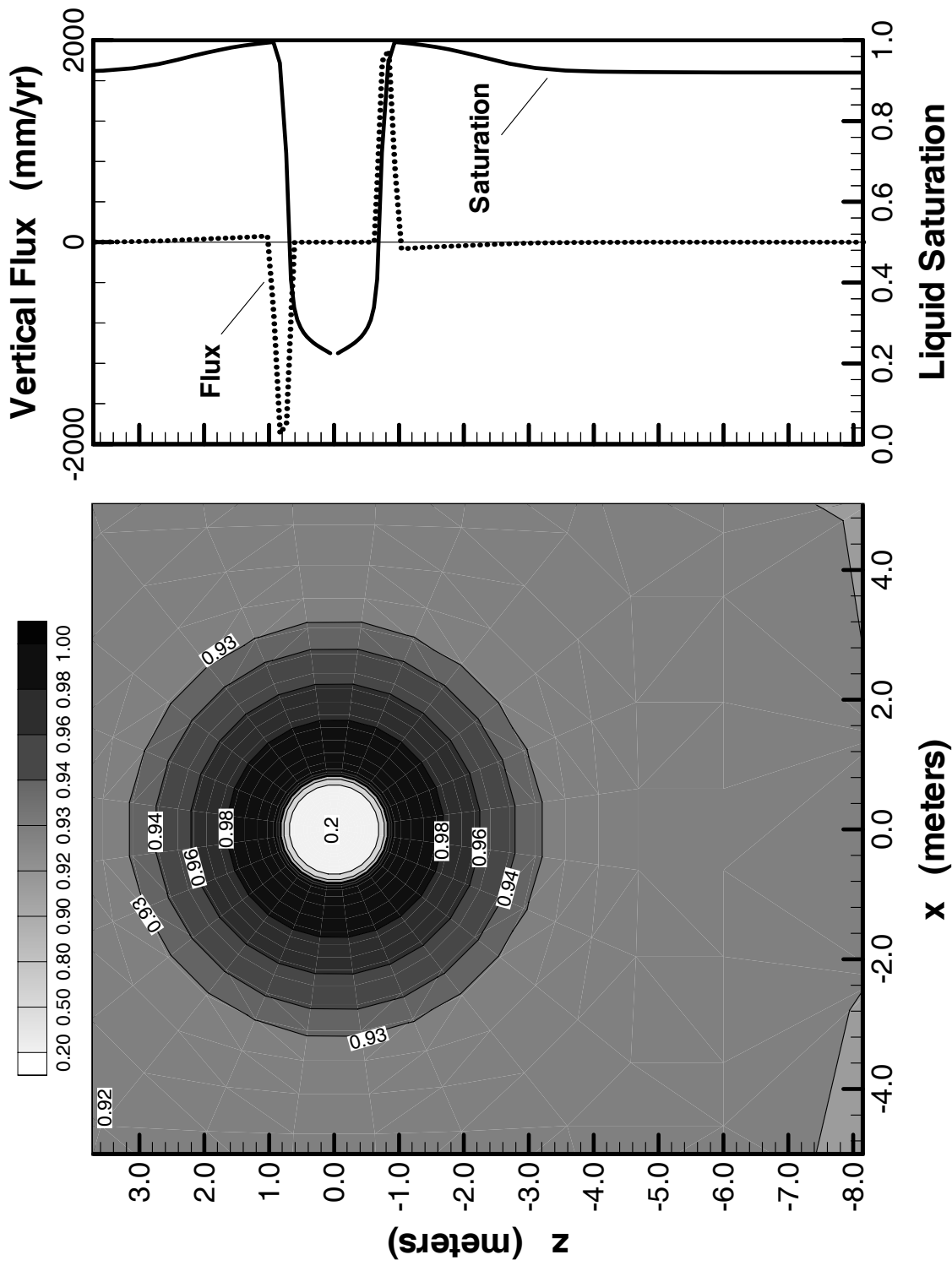


Figure 15. Matrix saturation and liquid flux at 3 months for simulation with the effective continuum model, shown for the center-plane of the SHT block. The xy-diagram shows distribution of saturation and flux along the z -axis at $x=0.0$ m. Positive flux values denote upward flow, negative flux values denote downward flow.

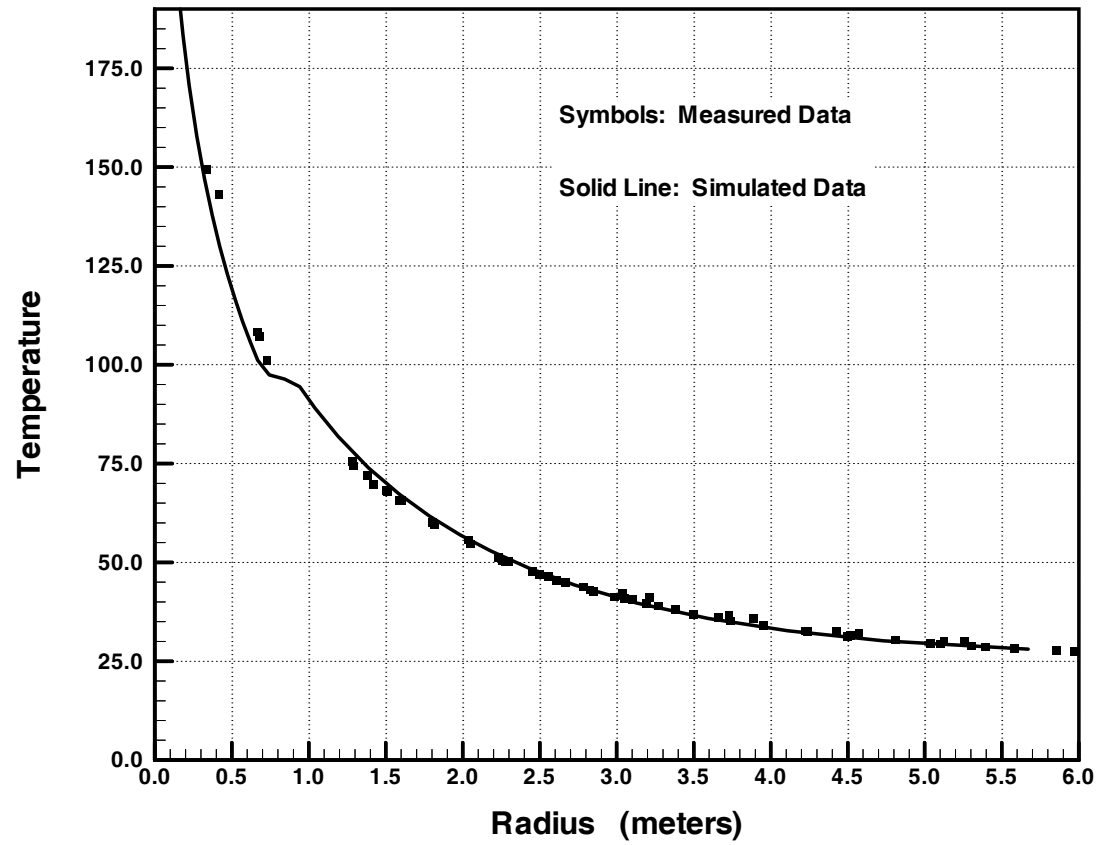


Figure 16. Measured and simulated temperature at 3 months, for the effective continuum conceptual model, for temperature sensors in the center-plane of the SHT block at $y = 4.5$ m.

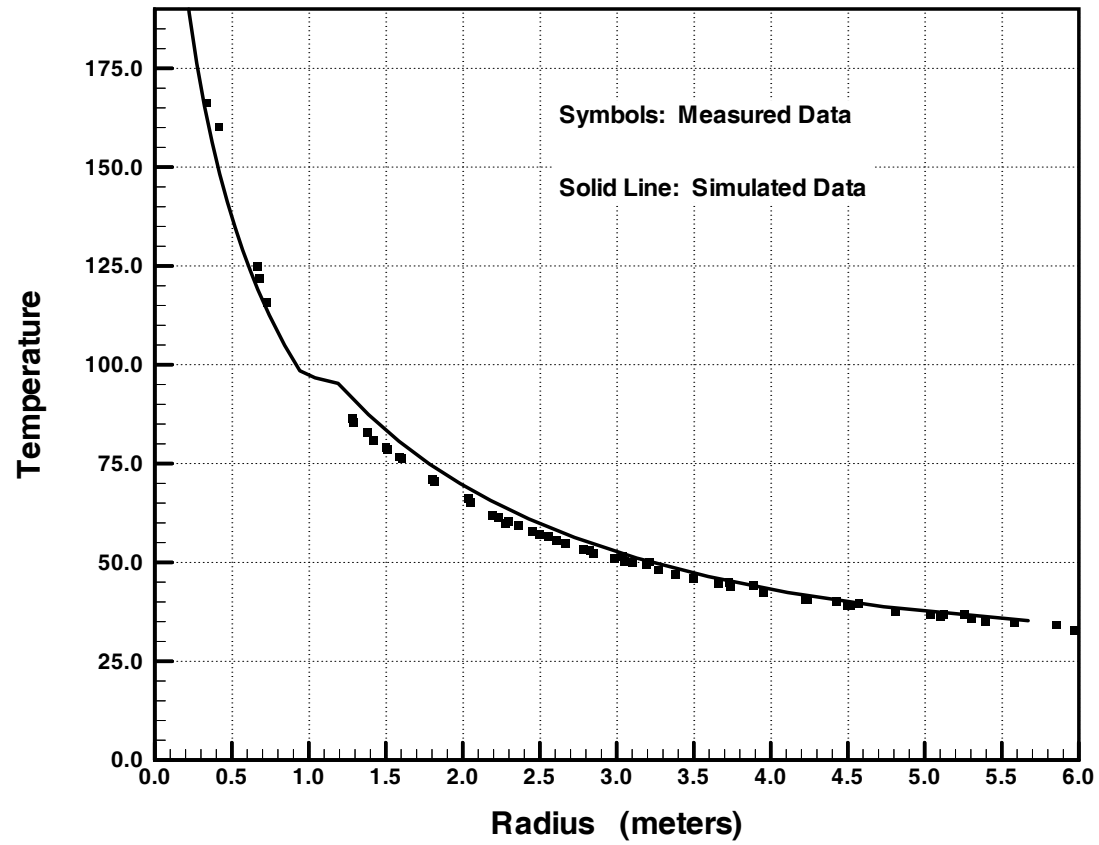


Figure 17. Measured and simulated temperature at 9 months, for the effective continuum conceptual model, for temperature sensors in the center-plane of the SHT block at $y = 4.5$ m.

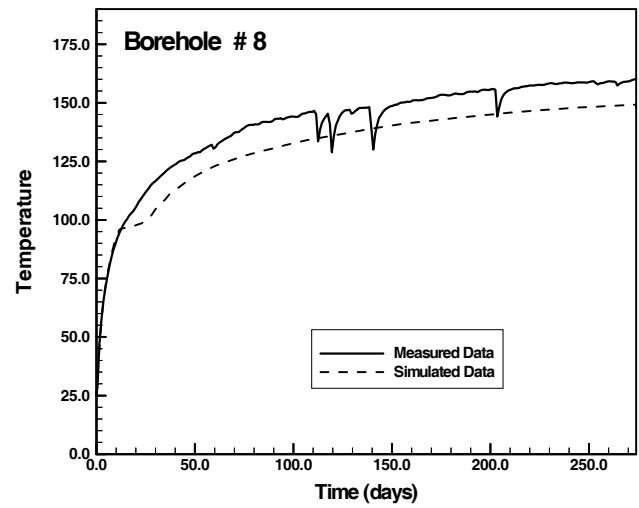
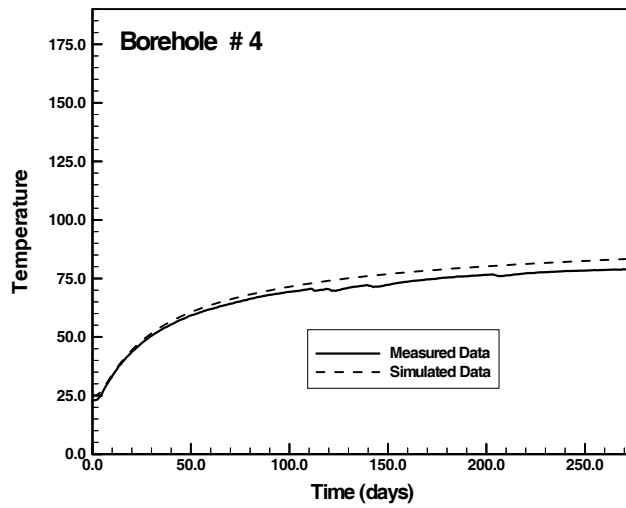
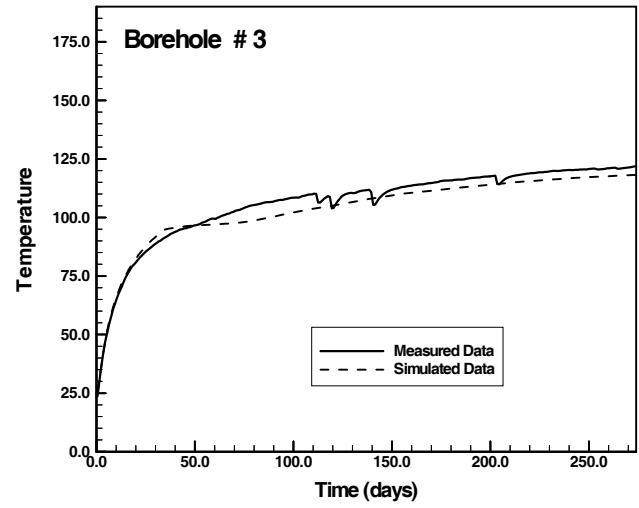
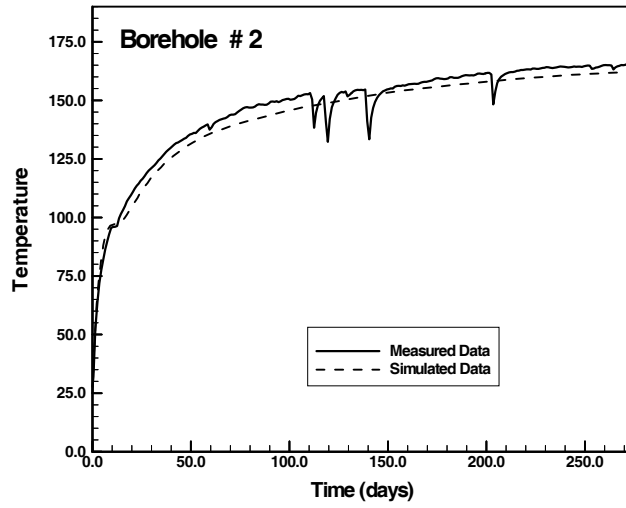
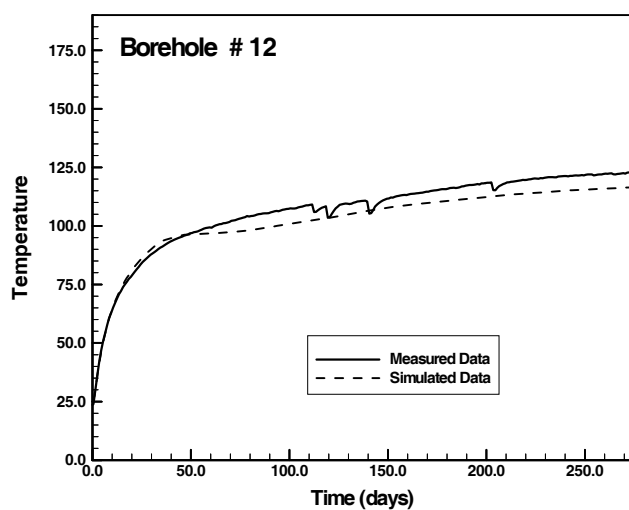
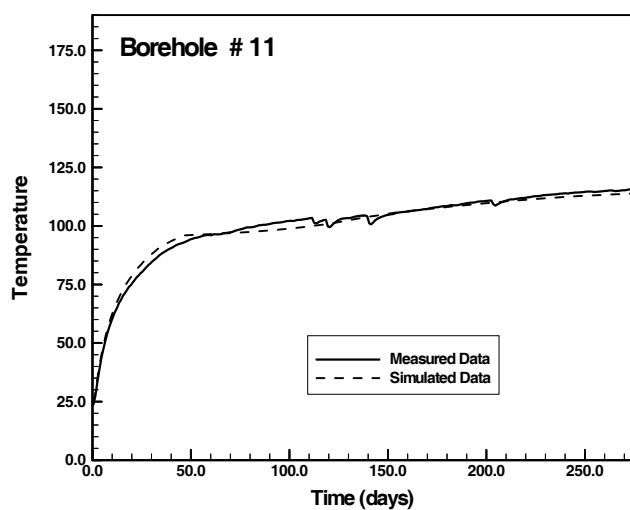
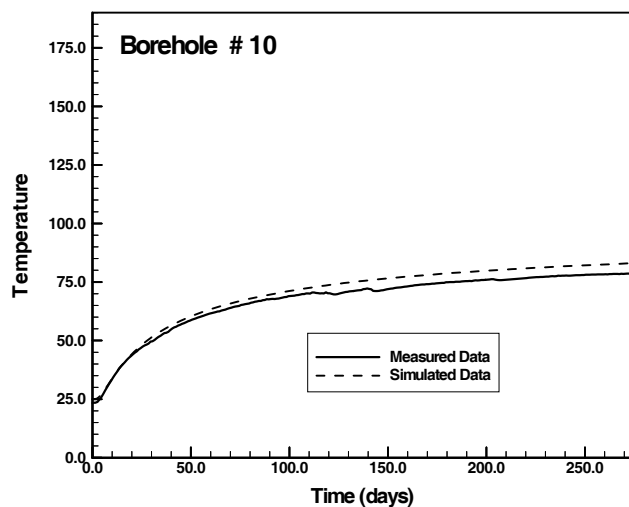
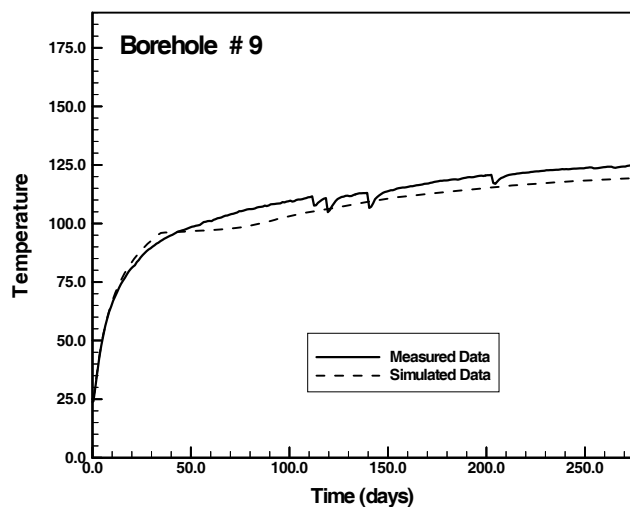


Figure 18. Measured and simulated temperature history, with the effective continuum conceptual model, for all boreholes parallel to Heater Hole 1, for temperature sensors in the center-plane of the SHT block.



cont. Figure 18. Measured and simulated temperature history, with the effective continuum conceptual model, for all boreholes parallel to Heater Hole 1, for temperature sensors in the center-plane of the SHT block.

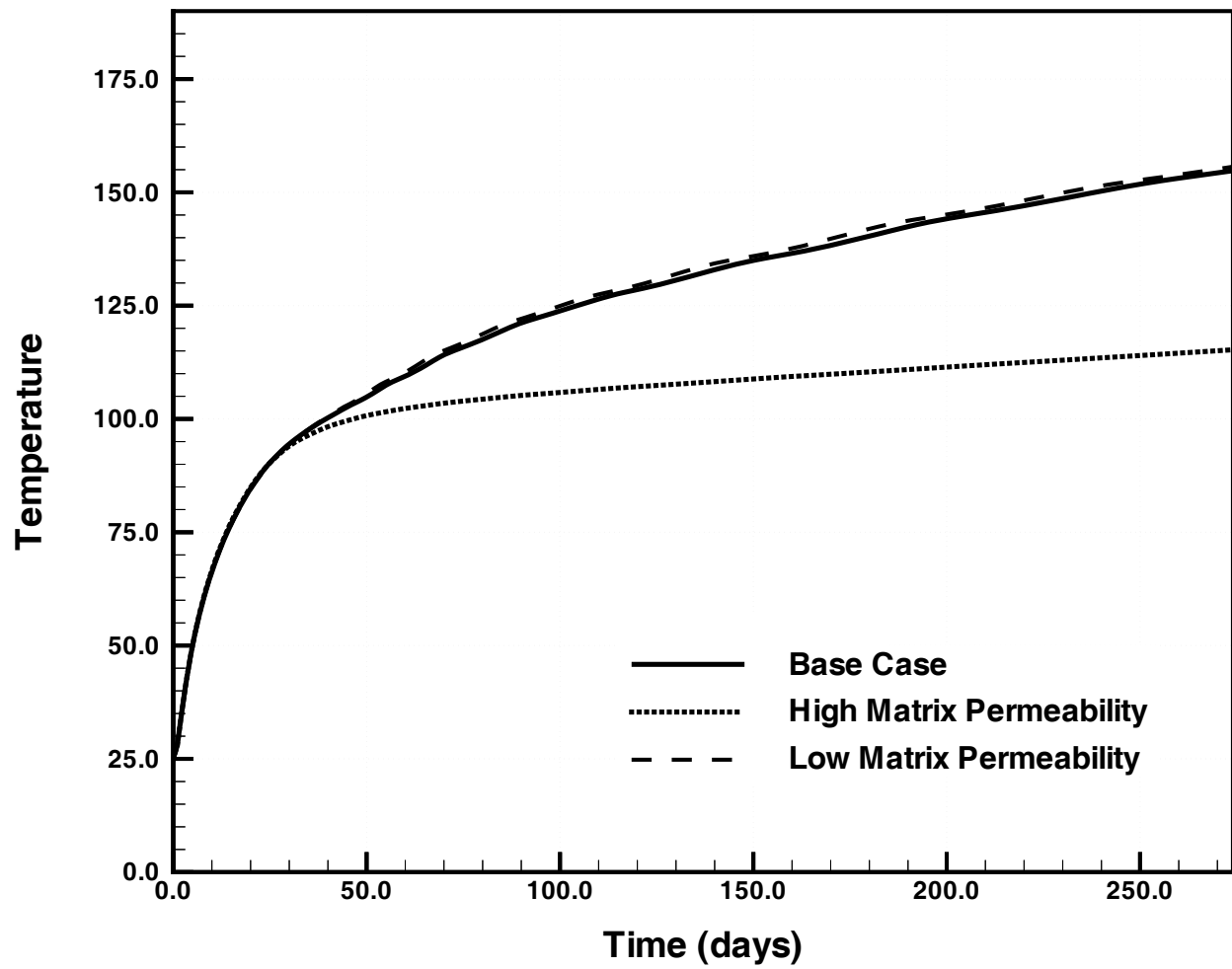


Figure 19. Sensitivity of temperature to matrix permeability, at a radial distance of 0.67 m from the heater. Simulation is for the dual permeability conceptual model in a x-z vertical plane at $y = 4.5$ m.

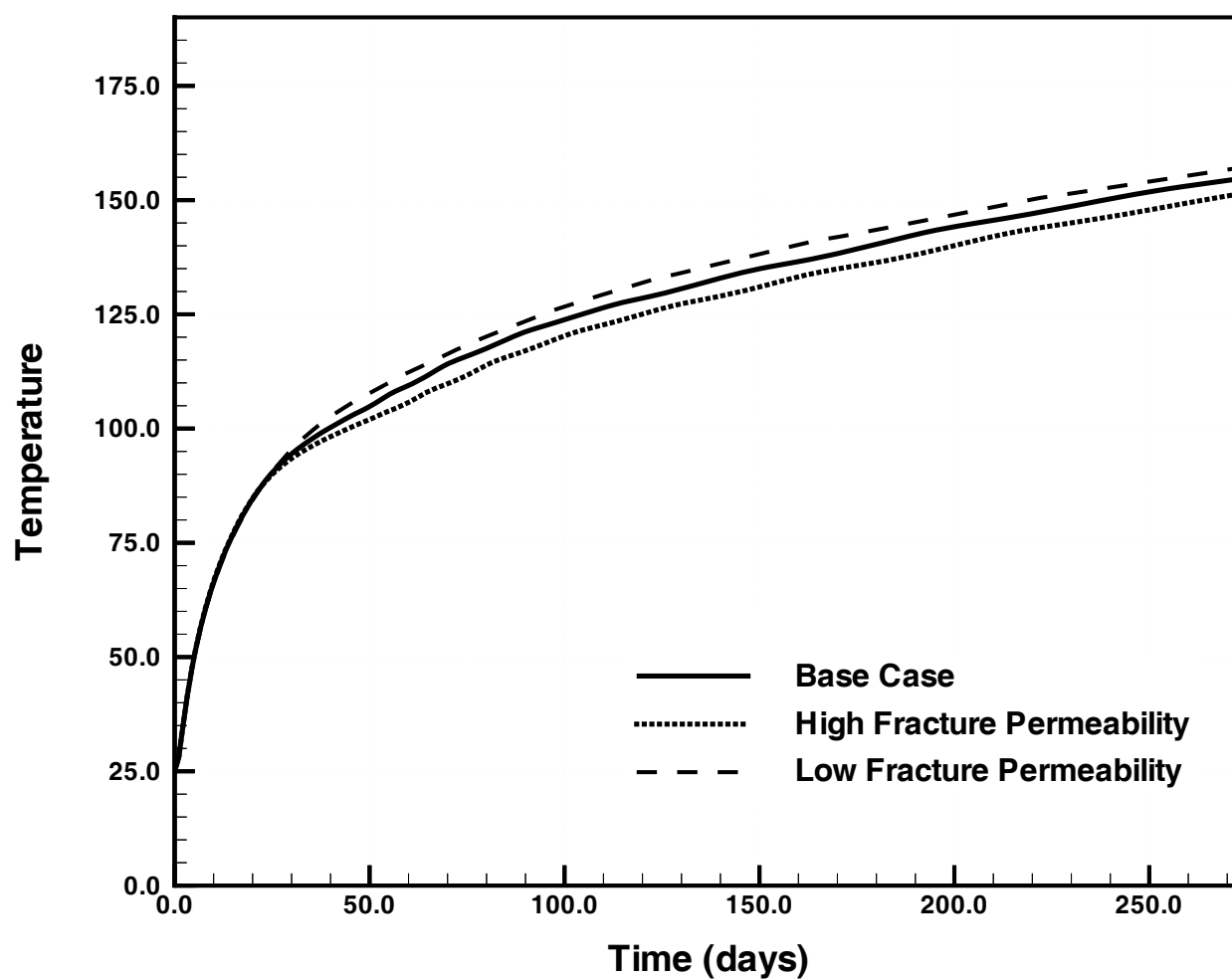


Figure 20. Sensitivity of temperature to fracture permeability, at a radial distance of 0.67 m from the heater. Simulation is for the dual permeability conceptual model in a x-z vertical plane at $y = 4.5$ m.

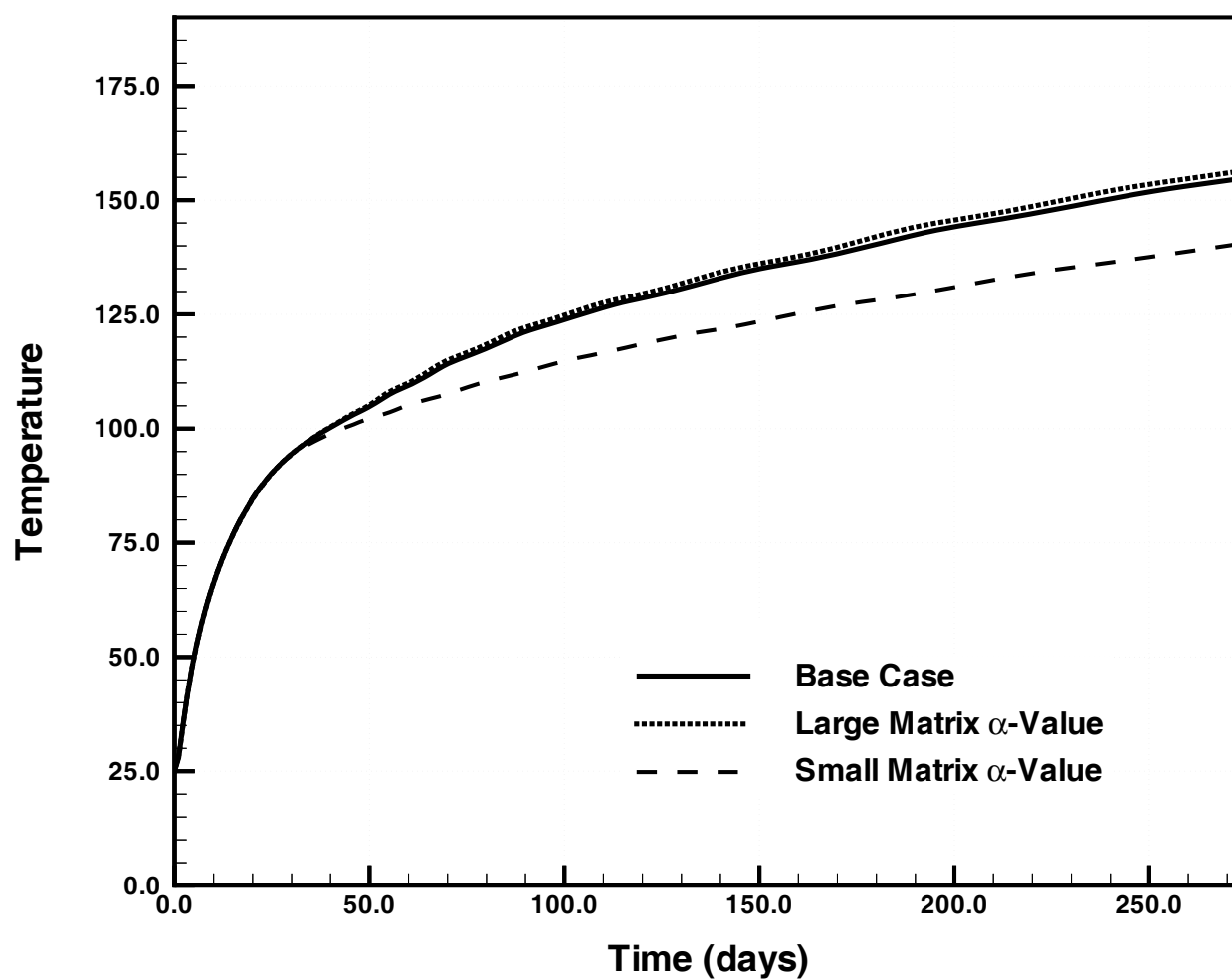


Figure 21. Sensitivity of temperature to matrix α parameter, at a radial distance of 0.67 m from the heater. Simulation is for the dual permeability conceptual model in a x-z vertical plane at $y = 4.5$ m.

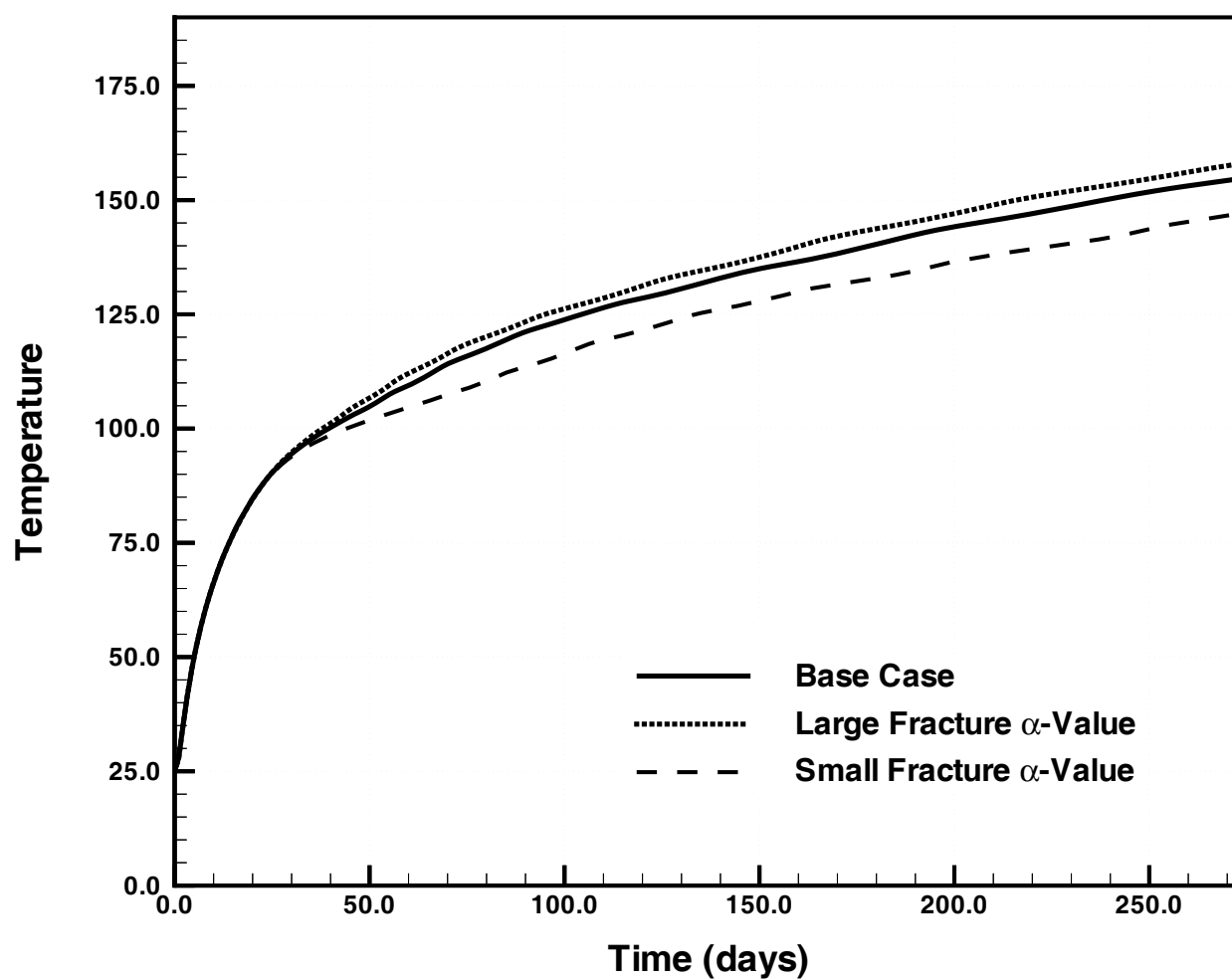


Figure 22. Sensitivity of temperature to fracture α parameter, at a radial distance of 0.67 m from the heater. Simulation is for the dual permeability conceptual model in a x-z vertical plane at $y = 4.5$ m.